Computers and Geotechnics 156 (2023) 105259

Contents lists available at ScienceDirect

Computers and Geotechnics

journal homepage: www.elsevier.com/locate/compgeo

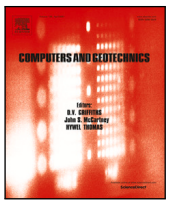

Research paper

Simulation of fully coupled hydro-mechanical behavior based on an analogy between hydraulic fracturing and heat conduction

Mingyao Li [a,b], Dong Zhou [a,*], Yewang Su [a,c,d,**]

[a] State Key Laboratory of Nonlinear Mechanics, Institute of Mechanics, Chinese Academy of Sciences, Beijing 100190, China
[b] State Key Laboratory of Coal Resources and Safe Mining, China University of Mining and Technology, Beijing 100083, China
[c] School of Engineering Science, University of Chinese Academy of Sciences, Beijing 100049, China
[d] State Key Laboratory of Structural Analysis for Industrial Equipment, Department of Engineering Mechanics, Dalian University of Technology, Dalian 116024, China

ARTICLE INFO

Keywords:
Hydraulic fracturing
Hydrothermal analogy
Fluid–solid coupling analysis
Finite element method
Numerical simulation

ABSTRACT

The hydraulic fracturing process involves complex coupling problems of the deformation and fracturing of solid and fluid flow in fractures. In this paper, a simple numerical tool for simulating the coupled hydro-mechanical behavior is developed by using an analogy between hydraulic fracturing and heat conduction. Using this analogy, the numerical implementation can be simply realized in the framework of a commercial finite element package ABAQUS with two user material subroutines to fully characterize the complex coupling problems of hydraulic fracturing. It is thus considerably simplified without any new development of user-defined element and fluid–solid solver but directly with the commercial finite element package. The proposed numerical tool along with the virtual crack method for elastic–brittle material is firstly verified by the classical 2D plain strain KGD analytical solution and then applied to several representative hydraulic fracturing problems and laboratory tests to illustrate its advantageous features. The present method is aiming to develop a useful numerical tool to study the coupled hydro-mechanical behavior of hydraulic fracturing. However, it is not limited to any specific materials and can be extended to other constitutive models that featured with the fully coupling problems of fluid and solid due to its simplicity.

1. Introduction

As the key technology in engineering practice for the exploitation of unconventional oil and gas resources, hydraulic fracturing has been extensively performed worldwide in recent decades (Montgomery and Smith, 2010). The increasing attention from the petroleum engineering appeals many researchers to investigate the complex process for characterization and development of oil and gas extraction. It is generally acknowledged that hydraulic fracturing is a complex multi-physics coupling process involving the mechanical deformation and fracturing of the shale formation, the fluid flow within the fractures and the coupling problems of fluid and solid (Osiptsov, 2017) as well as the proppant transport (Barboza et al., 2021). Several analytical solutions have been proposed to study the propagation of hydraulic fractures, however, only for some simplified fracture geometries, such as Khristinaovic-Geertsma–de Klerk (KGD) and Perkins–Kern–Nordgren (PKN) and other improved models (Detournay, 2004; Mitchell et al., 2006). The numerical models are thus progressively developed for more complex geometries and multi-physics process with the development of computational technology (Adachi et al., 2007). However, the numerical simulation of hydraulic fracturing is a tremendous challenge in particular the numerical treatment for the fully coupled hydro-mechanical behavior of the fluid flow and rock cracking (Chen et al., 2022).

Many research efforts have been devoted to developing different computational approaches to model the complex coupling system of hydraulic fracturing, such as displacement discontinuity method (DDM) (Olson and Dahi-Taleghani, 2009; Dong and de Pater, 2001; Xie et al., 2016; Kresse et al., 2013), finite element method (FEM) (Hunsweck et al., 2013; Devloo et al., 2006; Carrier and Granet, 2012), extended finite element method (XFEM) (Lecampion, 2009; Mohammadnejad and Khoei, 2013; Gordeliy and Peirce, 2013), discrete element method (DEM) (Al-Busaidi, 2005; Shimizu et al., 2011) as well as other emerging methods including phase field method (PFM) (Wilson and Landis, 2016; Mikelic et al., 2015; Miehe et al., 2015), discrete fracture network (DFN) (Fu et al., 2013; Dershowitz et al., 2010) and smeared crack model (SCM) (Hu et al., 2014; Li et al., 2016). To

* Corresponding author.
** Corresponding author at: State Key Laboratory of Nonlinear Mechanics, Institute of Mechanics, Chinese Academy of Sciences, Beijing 100190, China.
E-mail addresses: zhoudong@imech.ac.cn (D. Zhou), yewangsu@imech.ac.cn (Y. Su).

https://doi.org/10.1016/j.compgeo.2023.105259
Received 6 July 2022; Received in revised form 31 December 2022; Accepted 7 January 2023
Available online 12 January 2023

solve the complex coupling system successfully, two major concepts have been proposed to capture the rock fractures in the literature, i.e. discrete crack methods and continuum formulation based methods. The first class of the methods treats the crack as strong discontinuity in which the crack is real or equivalent to physical situation. However, these methods require advanced computational ability, especially for hydraulic fracturing with strong nonlinear coupling problems with the fluid flow (Shimizu et al., 2011). Alternatively, the approaches with continuum formulation, in which the crack is considered as continuously distributed form, have gained wide popularity. In contrast to the discrete crack models, these approaches regularize the crack discontinuities within a pure continuum formulation to avoid the difficulties of capturing the crack path evolutions associated with initiation, direction turning, as well as branching (Rahimi-Aghdam et al., 2019). This class of methods has been commonly applied in computational implementation in a straightforward manner. Among these approaches, the smeared crack model (SCM) treats the crack as an equivalent anisotropic continuum with degraded material properties in the direction normal to the crack orientation, and the remesh is avoided. However, the disadvantages of these methods are the inevitable difficulty of obtaining the crack information such as width and surface and handling the coupling problems of the fluid flow within the diffuse cracks. Alternatively, Chen et al. (2020) proposed an improved phase-field hydraulic fracturing model with a new FE-FV scheme and applied in simulating complex propagation of hydraulic fracture in naturally fractured formation. Therefore, large efforts still need to be made to handle these issues such as the difficulty of the numerical implementation of the interaction of pressurized fluids with crack surfaces.

In general, each type of approaches possesses its own advantages and disadvantages and the selected solution strongly depends on the requirements of the problems such as efficiency, accuracy or application. Among these methods, many efforts on the finite element method are based on the commercial package ABAQUS by its user subroutines to define the material's mechanical and other behaviors (Chau et al., 2016; Yao et al., 2015). For example, a user defined subroutine was developed to model the anisotropic damage behavior of shales (Chau et al., 2016) and a user-defined element was developed to treat the coupling problems of solid and fluid of multiple hydraulic fractures (Yao et al., 2015).

This paper develops an alternative method to study the fully coupled hydro-mechanical behavior of the fluid flow and rock fractures by an analogy between hydraulic fracturing and heat conduction. These two phenomena are completely different in nature, however, they can be mathematically treated the same by the concept of analogy which has been applied in many fields such as heat and mass transfer (Chung et al., 2021), diffusion and heat transfer (Duan et al., 2013), and thermal and electrical properties (Hao et al., 2018). Although the hydrothermal analogy is known in some literature (Bažant et al., 2014), the aim of this paper is to develop a simple and useful numerical tool by directly using the embedded heat conduction equations in a commercial finite element package ABAQUS without any new development of user-defined element and fluid–solid solver. Using this analogy, the numerical implementation can be realized in the framework of ABAQUS with two user material subroutines to fully characterize the complex coupling problems of hydraulic fracturing. Since this implementation does not involve any new development of user-defined element and fluid–solid solver, it is expected that the complex coupled hydro-mechanical behavior of the fluid flow and rock fractures of hydraulic fracturing can be thus considerably simplified. The present method is firstly validated by the classical KGD solution and then used to study several typical applications and laboratory tests of hydraulic fracturing problems.

2. Theory for hydraulic fracturing

The process of hydraulic fracturing involves the flow of fluid in cracks, the damage and crack opening of the shale and the coupling of each other. In this theory, the property of shale is modeled with damage mechanics and the cracks are considered in the smeared way by a concept of virtual crack method. The flow of fluid is modeled by the classic percolation theory with Lubrication equation. The pressure induced by the fluid affects the damage of the shale around cracks, which also changes the flow of fluid in return.

2.1. Deformation and fracturing of the shale

The property of shale is very complex due to the strongly anisotropic behavior related to the inherent mesostructure and damage mechanisms (Li et al., 2020). The failure of the shale, namely, the complete loss of loading carrying capacity, results from the progressive degradation of the material stiffness which can be modeled via damage mechanics. In this theory, the mechanical behavior of shale is characterized by an isotropic elastic damage constitutive law, as shown in Fig. 1(a). The maximum tensile strain criterion is assumed as the damage threshold while the compressive damage is not considered. Under uniaxial tension the stress–strain response follows a linear elastic relationship until the value of the critical strain is reached which corresponds to the onset of the micro-cracking. Beyond the damage threshold the damage progresses gradually until the breaking elastic strain which indicates fully damage in the shale formation. With respect to the constitutive law, the damage variable representing the degree of damage is proposed as:

$$w = \begin{cases} 0 & \varepsilon \le \varepsilon_{t0} \\ \frac{\varepsilon}{\varepsilon_{break}} & \varepsilon_{t0} \le \varepsilon \le \varepsilon_{break} \\ 1 & \varepsilon_{break} \le \varepsilon \end{cases} \tag{1}$$

where the damage variable w takes values from zero for the undamaged material to one for completely damage.

However, in this theory, the simulation of cracking process is attained via FEM as the basic stress analysis tool, where hexahedron element is used as the basic element in the finite element mesh and the elastic–brittle damage constitutive relationship (Fig. 1(b)) is adopted coupled with a concept of virtual crack model (Appendix A). In general, the element is considered to be linear-elastic until the maximum principle strain reaches a critical value, and a virtual crack in the element is assumed to take place in the normal direction. As the crack occurs, the element is assumed to be fully cracked in that direction corresponding to the brittle failure state of the elastic–brittle constitutive law, and thus the components of material stiffness matrix related to that direction are changed to zero. Three orthogonal cracks are allowed in one 3D element at most and the crack system is fixed as normal to the maximum principal strain at the time the cracks start to form and remain constant afterwards. However, the crack is assumed to be able to close and reopen according to the stress state, and the closed crack is able to support compressive loading but no shear ones. The arbitrary growth of the fractures can be modeled by changing the coefficient matrix of the constitutive relations. For more details, the simulation of the cracking process with FEM is referred to Appendix A.

It should be emphasized here that the following discussion is not specifically limited to the isotropic elastic–brittle constitutive model along with the virtual crack concept, the methodology can be applied to the general field theories to couple the fluid flow and rock fractures in hydraulic fracturing.

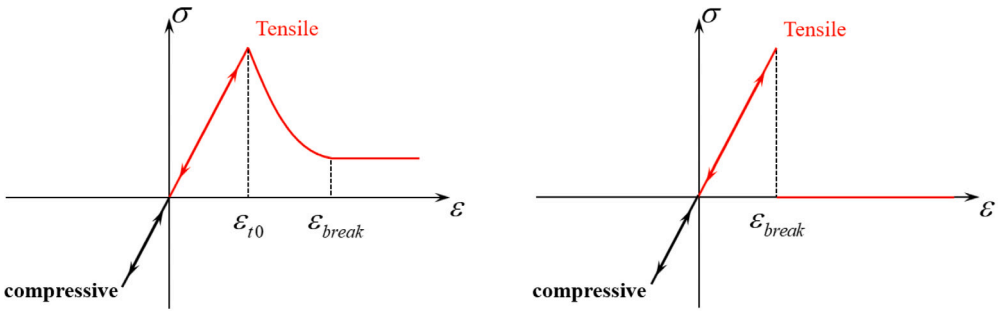

Fig. 1. Elastic damage constitutive law under uniaxial stress. (a) Strain softening with residual strength. (b) Brittle without residual strength.

2.2. Fluid flow through fractures

For fluid flowing in a single crack along x axis, Poiseuille law gives the relation between the volume discharge per unit width q and the pressure gradient as:

$$q = -\frac{h^3}{12\mu}\frac{\partial P}{\partial x} \tag{2}$$

where P is the fracking water pressure, h the crack aperture and μ the fluid viscosity.

In 3D space, the crack of a 2D plane and the direction of flow are not necessary to coincide with the global coordinates. Both the volume discharge and the pressure gradient are extended to vectors. Their relation becomes:

$$\boldsymbol{q} = -\boldsymbol{B}\cdot(\nabla P) \quad or \quad q_i = -B_{ij}\frac{\partial P}{\partial x_j} \tag{3}$$

where the second order permeability tensor $\boldsymbol{B}$ takes the form:

$$\boldsymbol{B} = \frac{h^3}{12\mu}(\boldsymbol{I} - \boldsymbol{n}\otimes\boldsymbol{n}) \quad or \quad B_{ij} = \frac{h^3}{12\mu}(\delta_{ij} - n_{ki}n_{nj}) \tag{4}$$

where $\boldsymbol{I} = \delta_{ij}\boldsymbol{e}_i\boldsymbol{e}_j$ is the unit tensor, $\boldsymbol{n} = n_i\boldsymbol{e}_i$ the unit normal direction of the crack plane, (e_1, e_2, e_3) the unit basis vectors of global coordinates.

In fact, two types of flow play a role in hydraulic fracturing, *i.e.* the flow inside the hydraulically fractures and the flow through the pores and intrinsic defects in shale. However, compared with the scale of hydraulically cracks, the pore-sizes in shale are typically in nanoscale (Josh et al., 2012), thus the fluid flow in porous media can be negligible as long as the hydraulic fractures form. Nevertheless, the effects of pores and initial defects should be taken into account for some phenomena, such as crack initiation and branching (Rahimi-Aghdam et al., 2019; Sun et al., 2021).

2.3. The effects of the shale damage to the flow of fluid

In general, three mutually orthogonal cracks are allowed in one 3D element (Fig. 2) and the crack opening widths are calculated from the principal inelastic strains $\varepsilon_1'', \varepsilon_2'', \varepsilon_3''$ in the form:

$$h_1 = l\langle\varepsilon_1''\rangle, h_2 = l\langle\varepsilon_2''\rangle, h_3 = l\langle\varepsilon_3''\rangle \tag{5}$$

where l is the material characteristic length which equals to the brick element size. The principal inelastic strains are calculated from the inelastic strains as follows:

$$\begin{aligned}
\varepsilon_1' &= \varepsilon_1 - \frac{\sigma_1 - \nu(\sigma_2+\sigma_3)}{E}\\
\varepsilon_2' &= \varepsilon_2 - \frac{\sigma_2 - \nu(\sigma_3+\sigma_1)}{E}\\
\varepsilon_3' &= \varepsilon_3 - \frac{\sigma_3 - \nu(\sigma_1+\sigma_2)}{E}\\
\varepsilon_4' &= \varepsilon_4 - \frac{(1+\nu)\sigma_4}{E}\\
\varepsilon_5' &= \varepsilon_5 - \frac{(1+\nu)\sigma_5}{E}\\
\varepsilon_6' &= \varepsilon_6 - \frac{(1+\nu)\sigma_6}{E}
\end{aligned} \tag{6}$$

where E and ν are Young's modulus and Poisson's ratio, respectively. σ_1, ε_i are the stress and strain components.

The flows within the three fractures are assumed to be independent of each other and the total permeability tensor of the element with three orthogonal cracks is the superposition of the contributions of these cracks:

$$\boldsymbol{B} = \frac{1}{12\mu}\sum_{k=1}^{3}h_k^3(\boldsymbol{I} - \boldsymbol{n}_k\otimes\boldsymbol{n}_k) \quad or \quad B_{ij} = \frac{1}{12\mu}\sum_{k=1}^{3}h_k^3(\delta_{ij} - n_{ki}n_{kj}) \tag{7}$$

$\boldsymbol{n}_k = n_{ki}\boldsymbol{e}_i$ is the direction of the principal inelastic strain. Thus, the crack widths change the permeability tensor relating to the fluid flow in the shale to affect the fluid flow with the change of the distribution of the pressure in the fluid.

2.4. The effects of the flow of fluid to the shale damage

Meanwhile, the changing distribution of the fluid pressure in turn affects the stresses and crack widths in the shale which also in turn affect the fluid flow and pressure. The effects of fluid flow on the deformation of shale are treated as an additional stress σ^A on the walls of each crack separately:

$$\begin{aligned}
\boldsymbol{\sigma}^A &= -\sum_{k=1}^{3}[(Pw_k\boldsymbol{n}_k\otimes\boldsymbol{n}_k) + Pw_k\frac{h_k}{l+h_k}(\boldsymbol{I} - \boldsymbol{n}_k\otimes\boldsymbol{n}_k)] \quad or\\
\sigma_{ij}^A &= -\sum_{k=1}^{3}[Pw_kn_{ki}n_{kj} + Pw_k\frac{h_k}{l+h_k}(\delta_{ij} - n_{ki}n_{kj})]
\end{aligned} \tag{8}$$

where w_k is a variable representing the degree of damage with respect to the elastic–brittle constitutive relationship (Fig. 1(b)):

$$w_k = \begin{cases} 0 & \varepsilon_k'' \le \varepsilon_{k,break}'' \\ 1 & \varepsilon_k'' \ge \varepsilon_{k,break}'' \end{cases} \tag{9}$$

where the damage variable indicates no damage as the principal inelastic strain not exceeding the critical breaking inelastic strain $\varepsilon_{k,break}''$ and fully damage on the other hand.

2.5. Governing equations for the flow of fluid

The principle of fluid mass conservation gives the following continuity equation:

$$\frac{\partial(\rho h)}{\partial t} + \frac{\partial(\rho q_i)}{\partial x_i} = 0 \tag{10}$$

where $h = h_1 + h_2 + h_3$ is the summation of the crack width. The fracturing water is considered to be compressible and the mass density of the fluid depends on the pressure and takes the form:

$$\rho = \rho_0(1 + \frac{P}{K}) \tag{11}$$

where ρ_0 is the mass density at reference pressure P and K is the volumetric modulus of fracking fluid. It is noted that the mass density

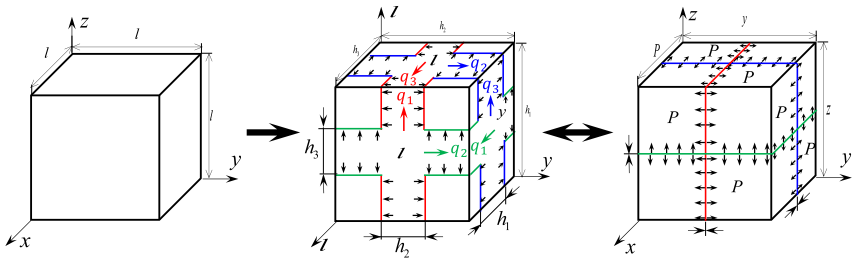

Fig. 2. Three orthogonal cracks system and evolution pattern with flow and pressure distribution in a 3D element. (a) Intact element. (b) Cracked element with flow and pressure inside. (c) Closed cracked element with pressure inside.

Table 1
Analogy between hydraulic fracturing and heat conduction.

Hydraulic fracturing	Heat conduction	Analogy
Mass flow rate: $M_i = -k_{ij}\frac{\partial P}{\partial x_j}$	Fourier law: $q_i = -k_{ij}\frac{\partial T}{\partial x_j}$	$q_i = M_i$ $T = P$
Mass conservation: $\rho_0\frac{\partial V}{\partial t} + \frac{\partial M_i}{\partial x_i} = 0$	Thermal energy conservation: $\rho\frac{\partial U}{\partial t} + \frac{\partial q_i}{\partial x_i} = 0$	$\rho = \rho_0$
Governing equation: $\rho_0\frac{\partial V}{\partial t} - \frac{\partial}{\partial x_i}[k_{ij}\frac{\partial P}{\partial x_j}] = 0$	Governing equation: $\rho\frac{\partial U}{\partial t} - \frac{\partial}{\partial x_i}(k_{ij}\frac{\partial T}{\partial x_j}) = 0$	$U = V$

of the fluid $\rho = \rho_0$ if the fluid is incompressible with infinite large volumetric modulus.

Combining Eqs. (3), (10) and (11) gives the diffusion equation for the flow of fracking fluid though shale as follows:

$$\rho_0\frac{h}{K}\frac{\partial P}{\partial t} - \rho_0\frac{\partial}{\partial x_i}[(1+\frac{P}{K})B_{ij}\frac{\partial P}{\partial x_j}] + \rho_0(1+\frac{P}{K})\frac{\partial h}{\partial t} = 0 \tag{12}$$

3. Analogy between hydraulic fracturing and heat conduction

In general, the governing equation for the fluid flow in hydraulic fracturing can be derived as:

$$\rho_0\frac{\partial V}{\partial t} - \frac{\partial}{\partial x_i}[k_{ij}\frac{\partial P}{\partial x_j}] = 0 \tag{13}$$

from the mass flow rate $M_i = -k_{ij}\partial P/\partial x_j$ and the conservation of mass $\rho_0\partial V/\partial t + \partial M_i/\partial x_i = 0$, where $k_{ij} = \rho_0(1+P/K)B_{ij}$ is the coefficient of the flow, as known as hydraulic conductivity, V the fluid volume within the fracture, ρ the fluid density, K the fluid volumetric modulus. The relations between these variables are summarized as $\rho = \rho_0(1+P/K), V = h(1+P/K), \partial V/\partial P = h/K$.

Accordingly, the governing equation of the heat conduction takes the form as:

$$\rho\frac{\partial U}{\partial t} - \frac{\partial}{\partial x_i}(k_{ij}\frac{\partial T}{\partial x_j}) = 0 \tag{14}$$

with the heat flux $q_i = -k_{ij}\partial T/\partial x_j$ and the conservation of heat $\rho\partial U/\partial t + \partial q_i/\partial x_i = 0$, in which k_{ij} is the thermal conductivity, T the temperature, U the internal heat energy and ρ the density.

By comparing Eqs. (13) and (14), the hydraulic fracturing and the heat conduction can be analogized by the following equivalence in Table 1.

The initial and boundary conditions can be analogized as:

$$T = \bar{T}_0 \Leftrightarrow P = \bar{P}_0 \tag{15}$$

$$\left.\begin{array}{c} T = \bar{T}, \quad at\ \Gamma_1 \\ q_i n_i = -\bar{q}, \quad at\ \Gamma_2 \\ q_i n_i = -\alpha^T(\bar{T}-T), \ at\ \Gamma_3 \end{array}\right\} \Leftrightarrow \left\{\begin{array}{c} P = \bar{P}, at\ \Gamma_1 \\ M_i n_i = -\bar{M}, at\ \Gamma_2 \\ M_i n_i = \alpha^P(\bar{P}-P), at\ \Gamma_3 \end{array}\right. \tag{16}$$

where $\bar{T}_0, \bar{P}_0$ are the initial temperature and fluid pressure, $\Gamma_1, \Gamma_2, \Gamma_3$ denote the first, second and third boundary conditions with the boundary values $\bar{T}$ for temperature and $\bar{q}$ for heat flux, and boundary values $\bar{P}, \bar{M}$ for fluid pressure and mass flow rate, and α^T and α^P the thermal and fluid coefficient of diffusion. Thus, the analogy between hydraulic fracturing and heat conduction is mathematical established from governing equations as well as initial and boundary conditions.

Using this analogy, the fluid flow in hydraulic fracturing process can be realized through coupled heat transfer and deformation by defining specific heat transfer behavior (UMATHT) for the fluid flow and mechanical constitutive relations (UMAT) for solid formation. The fully-coupled temp-displacement analysis can be utilized to fully couple the fluid flow and solid deformation with the specific coupled temperature–displacement element type in ABAQUS. Therefore, the challenge of numerical implementation is significantly simplified without any further development of user-defined element (UEL) and fluid–solid solver.

4. Numerical implementations

To this end, the proposed method is completely developed for the numerical simulation of hydraulic fracturing based on the simplified numerical tool by the analogy between the hydraulic fracturing and heat conduction. The flow chart of the solving procedure for hydraulic fracturing is illustrated in Fig. 3. After initialization the strain vector ε_i is updated at $t+\Delta t$ and the crack directions n_{ki} are updated according to the state of the last step. If there is no crack the rotation matrix T_{ij} will be unit matrix and the strain vector ε_i^p at crack system will be the same as the total strain vector. Otherwise, the strain vector will be updated according to the crack system at last step and the updated strain vector will be utilized to determine the new state of element and new crack directions. The local stiffness matrix D_{ij}^L can be determined by the state of element and the global stiffness matrix D_{ij}^G can be calculated by the rotation matrix T_{ij} in the function of the crack directions. The procedure in the red box is basically the coupling of virtual crack system and elastic–brittle constitutive model. After determination of these variables the fully coupled process is then required within each time step by the exchange of the crack width h_k, flow coefficient B_{ij} and the fluid pressure P which are so-called coupling parameters. Specifically, the crack width h_k and the flow coefficient B_{ij} can be then calculated and transferred to the fluid flow part by the common block. The additional stress σ_{ij}^A induced by the fluid pressure within the crack can be calculated by the state of the element and the fluid pressure P transferred back from fluid flow part. It is noted that we calculate the incremental additional stress by the difference between the additional stress at current step and the previous step in order to avoid the new sudden fracture at current step. Finally, the total stress $\sigma_{i(t+\Delta t)}$ is updated with three stresses including the former stress $\sigma_{i(t)}$, the incremental constitutive stress $d\sigma_{i(t+\Delta t)}^c$ and the incremental additional stress $d\sigma_{i(t+\Delta t)}^A$. The Jacobian matrix is lastly updated according to the stiffness matrix of the element at current state. It is worth noting that the stiffness matrix related to the state of the element with different fractures dose not destroy the original structure which is suitable to update the Jacobian matrix.

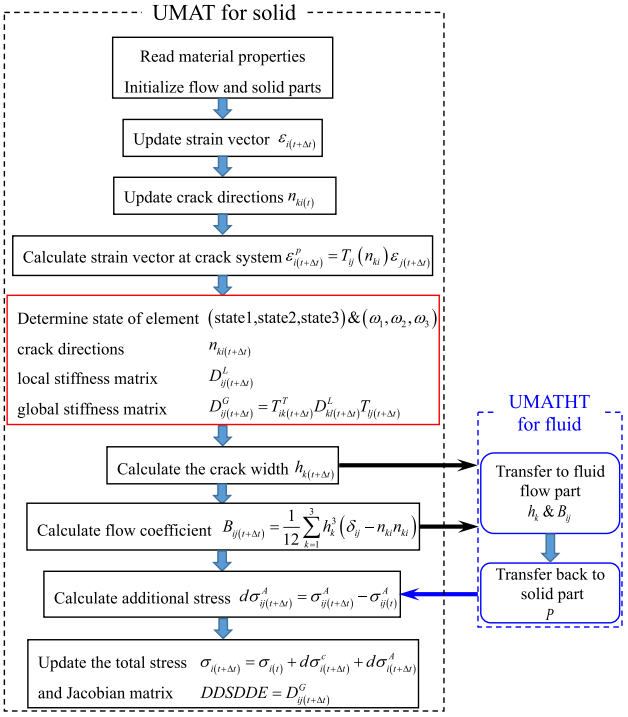

Fig. 3. Flowchart of the interaction between UMAT and UMATHT for fully coupled hydro-mechanical problem.

Table 2
Material parameters used for the numerical simulations and KGD analytical solution.

Young's modulus E (GPa)	20.0
Poisson's ratio ν	0.20
Injection rate q (m^3/s)	1.0×10^{-5}
Volumetric modulus K (GPa)	0.08
Dynamic viscosity μ (mPa s)	1.01
Model height h (m)	0.1
Breaking strain ϵ_k	0.00025

5. Verification

In this section, the performance of the proposed numerical treatment for hydraulic fracturing is preliminarily verified by the classic KGD analytical solution (Geertsma and de Klerk, 1969; Mohammadnejad and Khoei, 2013). The KGD model is assumed to be a 2D-plain-strain problem with homogeneous and isotropic formation which is characterized by the Young's modulus E and Poisson's ratio ν. The fluid is injected at a constant rate q which generates an elliptical fracture in horizontal cross-section with a constant height h of rectangular shape in vertical cross-section. The fluid flow with dynamic viscosity μ inside the fracture can be described with the smooth parallel-plate mode without considering the fluid leak off. With these assumptions the maximum fracture aperture w_{max} and the maximum net fluid pressure $p_{net,max}$ in the fracture can be calculated using the following equation:

$$w_{max} = 2.36\left(\frac{q^3\mu}{E'h^3}\right)^{1/6} t^{1/3}$$
$$p_{net.max} = 1.09(E'^2\mu)^{1/3} t^{-1/3} \tag{17}$$

where $E' = E/(1-\nu^2)$ is the plain strain modulus. The material parameters used for the verification are listed in Table 2.

The numerical model has a dimension of 10.1 m × 10 m × 0.1 m and each element has a dimension of 0.1 m × 0.1 m × 0.1 m as shown in Fig. 4(a). In order to be consistent with the KGD model the plain strain boundary conditions are applied to the model and symmetric boundary condition is applied to the left side with injection hole. A constant injection rate q is performed and the simulation results of hydraulic fracturing for different times are illustrated in Fig. 4(b) and (c). The comparison between the numerical simulation and the classic KGD analytical solution for the maximum fracture aperture and the maximum net fluid pressure are shown in Fig. 5. As can be seen that the prediction of the maximum fracture aperture provided by the proposed method is nearly in agreement with the KGD analytical solution with slightly difference. However, the prediction underestimates the maximum net fluid pressure and overestimates the remaining net fluid pressure in the fracture. It is mainly due to the initial pressure of the injection point which reduces the effect of the fluid pressure which is the limitation of the present model. Due to the limitations of the present computational capacity, a more thorough verification could be made in future such as large size of the domain, the mesh sizes and the fracture length. Thus, the present model is validated by the classical KGD solutions for the further investigations.

6. Numerical results and analysis

The present method is expected to be a useful numerical tool to study related problems due to its simplicity and can be extended to other constitutive models to solve the cracking process. In this section, some representative numerical examples of the hydraulic fracturing are analyzed and discussed based on the material parameters listed in Table 2.

6.1. Simulation of multiple simultaneous hydraulic cracking

Simultaneous hydraulic fracturing is the current preferred method of completion of horizontal wells in unconventional oil and gas extraction. However, the propagation of multiple simultaneous hydraulic fractures is strongly affected by the fracking water pressure as well as the interactions among each other. For this purpose, two-dimensional horizontal layers of shale with multiple perforations are investigated. It must be noted that two categories of simultaneous hydraulic cracking are take into account to obviate the effects of boundary conditions: finite cracks and infinite cracks.

For the case of finite cracks, the geometry is shown in the leftmost graph of Fig. 6(a) for three perforations and (b) for five ones on the left side of the model. As for the boundary conditions, the left side is set to be symmetric about x-axis ($u_x = 0$), and fixed on the other sides ($u_x = 0, u_y = 0$). Two types of boundary conditions are analyzed for the top and bottom sides, i.e. (1) fixed boundary ($u_x = 0, u_y = 0$) and (2) no constraint boundary. Meanwhile, the distance between the top/bottom boundary and the outmost perforations is set to be 10 times of perforation spacing to exclude the possibility of the effects from the boundaries of the model. The size of the model thus varies with the perforation spacing and three typical spacing are studied, namely, 2 m, 4 m and 10 m. The crack propagation and distribution of fluid pressure are visualized in the middle graphs of Fig. 6(a) and (b). One can observe that the fluid flow barely starts to develop crack at the interior borehole but the cracks from the exterior ones propagate smoothly until hit the boundary. It is noted that the stress distribution near the perforations is the same at the primary state, however, as the fluid pressure increase the interior one is clearly suppressed by the other two which is the reason why the interior crack rarely propagates. The results remain the same for different boundary conditions and different numbers and spaces of perforations. For further analysis of the reason, the critical strain values at the moment of crack initiation are recorded in the rightmost graph Fig. 6(a) and (b). It is found that the critical strains of the center perforations for all conditions are constantly less than the values of the exterior perforations. The main reason is that the fluid pressures from the exterior perforations compress on the interior ones to restrain its propagation which is so called stress shadow effect. It is noteworthy that the stress interaction is decreasing with large fractures

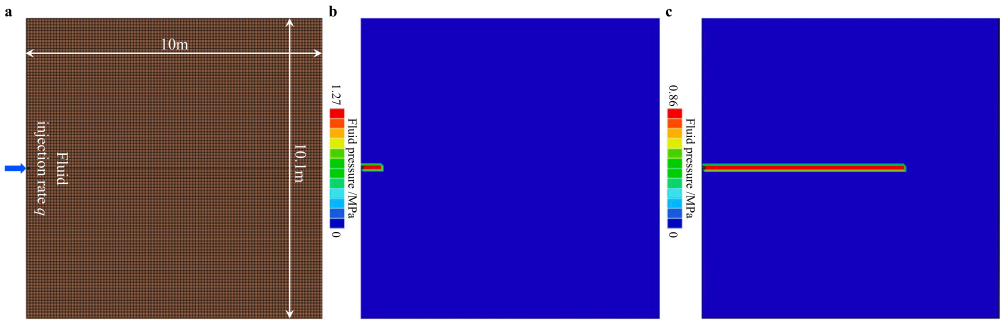

Fig. 4. Numerical simulation of the hydraulic fracturing for the KGD model. (a) Geometry of the model. (b) Crack propagation and fluid pressure distribution with the crack at 47 s. (c) Crack propagation and fluid pressure distribution with the crack at 100 s.

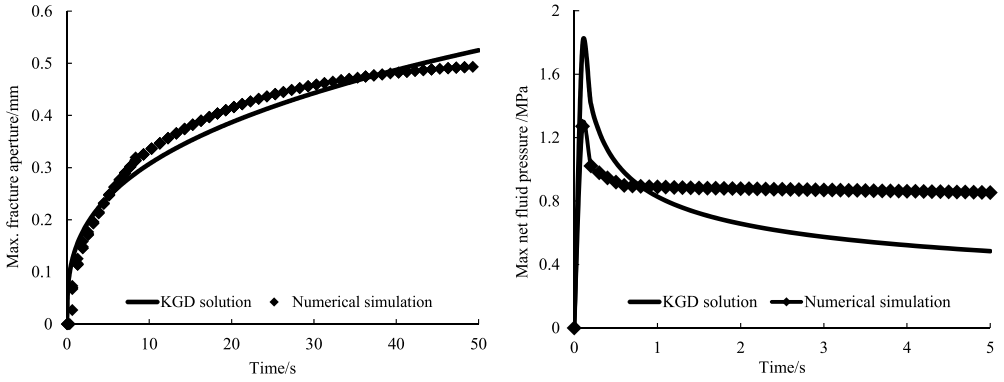

Fig. 5. Validation of the proposed model using the KGD analytical solution. (a) Comparison of the maximum fracture aperture. (b) Comparison of the maximum net fluid pressure.

spacing and there is only a marginal difference between the critical strain values as the cracks spacing increases to 10 m. Additionally, even though the fractures propagate along nearly straight paths, the fluid flow inside the cracks indeed influences each other to inclined angles. The curved crack paths can be more evident as the numerical model is further improved to avoid the mesh sensitivity in the future work. The results in this study are consistent with the works of other researchers (Zeng et al., 2017; Olson, 2008).

For the case of infinite cracks, the numerical results are quite different from the ones of finite cracks. As illustrated in the leftmost graph of Fig. 6(c) for three perforations and (d) for five ones, symmetric boundary conditions are applied on all sides of the model and the distance between the exterior perforations and the up/bottom boundary is set to be half perforation spacing. It is noteworthy that the multiple fractures propagate randomly for different perforation spacings which is entirely different from the results of the finite cracks. For the case of three boreholes the center one propagates but the two outer ones are stunted when the perforation spacing is 2 m. However, when the perforation spacing is 4 m and 10 m the outer cracks propagate but the center one is suppressed (Fig. 6(c)). Similarly, the pattern of cracks propagation for five perforations is also random as depicted in the middle graphs of Fig. 6(d). The critical strain values are listed in rightmost graph of Fig. 6(c) and (d) for further analysis and it must be noted that the critical values are identical for all cases. In other words, the stress states for different cracks are completely same when the symmetric geometry and boundary conditions are performed. Therefore, the effects of stress shadow are excluded but the issue of stability of multiple cracks propagation arises. Strictly, although the listed critical strain values are the same, infinitesimal difference is numerically inevitable which finally leads to randomly instable crack propagation. Little relevant research is found except the contribution in Bažant and Ohtsubo (1977) and Bažant et al. (1979), the stability of multiple parallel cracks under geothermal conditions is analyzed from theoretical perspective but no numerical results and the final solution. To some extent, our research findings provide a reasonable interpretation for instable crack propagation caused by the physical perforations in practical engineering and further solution is proposed in the following section.

6.2. Effects of the notches

As stated in Section 6.1 stress interference and instability should be avoided to create as many simultaneous multiple hydraulic fractures as possible in practical engineering. It is found in this study that the initial notch length can strongly influence the propagation pattern of a system of cracks to a certain extent. The same models are performed in Fig. 7(a) and (c) and the notches with an additional element to model the long initial length of the notches are also studied as shown in Fig. 7(b) and (d). It is noted that for the short ones the numerical results are random as same as the ones in the former section, but for the long initial length indicated by red circle in Fig. 7 the crack always propagates at the notches with long initial length. Namely, the crack propagation is no longer dominated by the stress interaction and instability but preferred to propagate from the notches with long initial length. Therefore, the research results provide a practical solution to overcome the effects of stress interaction and instability by introducing proactive length to control the hydraulic fracturing in advance.

6.3. Effects of in-situ stresses

Now consider a cross-section of a vertical wellbore with size 5 m × 5 m and a center hole of 0.1 m × 0.1 m as depicted in Fig. 8. The horizontal minimum and maximum principal stress is 5 MPa and 10 MPa, respectively. The fluid flow is injected from the center perforation with the same pressure history as before. It is shown from the distribution of the fluid pressure that the hydraulically induced crack propagates perpendicular to the direction of the minimum horizontal principal stress (Fig. 8(b)). The influence of the difference of the two-horizontal

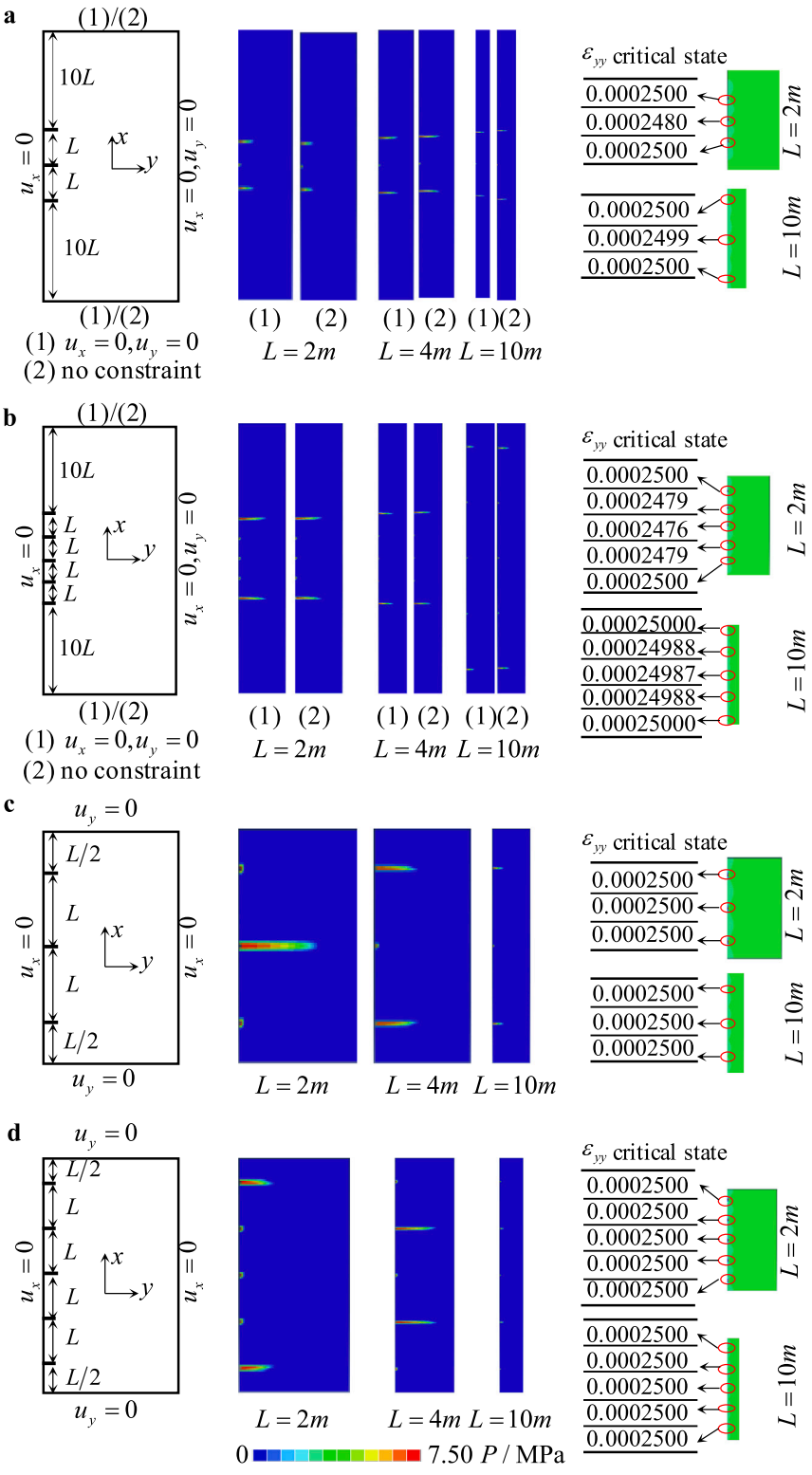

Fig. 6. Simulation of multiple simultaneous hydraulic fracturing with different number of perforations, boundary conditions and perforation spacing. (a) Finite cracks with three perforations. (b) Finite cracks with five perforations. (c) Infinite cracks with three perforations. (d) Infinite cracks with five perforations.

stress is investigated and it is noted from Fig. 8(c) that the breakdown pressure decreases with the increase of the horizontal stress difference.

6.4. Three-dimensional simulation of one hydraulic fracturing

A three-dimensional cubic block with size of 1.1 m × 1.1 m × 1.1 m with one perforation at center is now studied to verifying the proposed model for 3D cases. All boundaries are mechanically fixed, and the other parameters are the same. The geostresses are σ_h = 5 MPa, σ_H = 0 MPa, σ_v = 10 MPa as illustrated in Fig. 9(a). The distribution of fluid pressure on the two vertical cuts of the block is shown in Fig. 9(b) and one can observe clearly a penny-shaped crack and the propagation path is perpendicular to the direction of the minimum horizontal geostress. In order to show clearly the shape of the crack, the snapshots of the

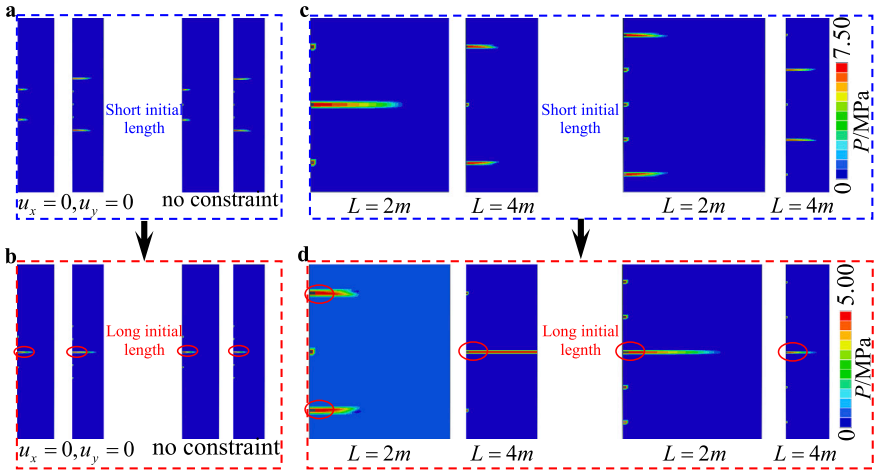

Fig. 7. Effects of the initial notch length with different numbers, boundary conditions and spacings (a) Finite cracks with short initial length. (b) Finite cracks with long initial length. (c) Infinite cracks with short initial length. (d) Infinite cracks with long initial length.

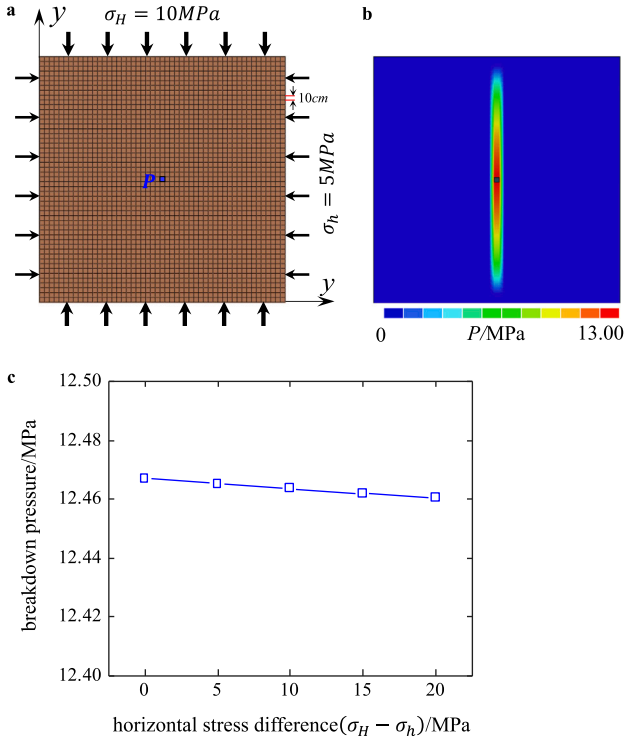

Fig. 8. Effects of in-situ stresses. (a) Geometry and in-situ stresses. (b) Crack propagation and distribution of the fluid pressure. (c) Influence of the difference of the two-horizontal stress on breakdown pressure.

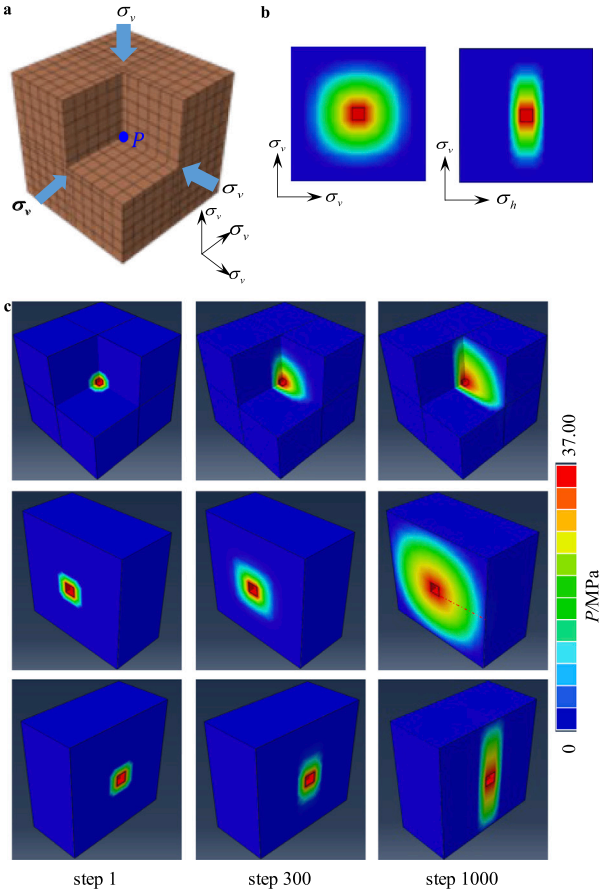

Fig. 9. Three-dimensional simulation of one hydraulic fracturing. (a) Geometry and in situ stresses. (b) Distribution of fluid pressure on the two vertical cuts of the block. (c) Snapshots of the fluid pressure on different cuts at different time steps.

fluid pressure patterns on the different cuts at different time steps are illustrated in Fig. 9(c). It is noted that with the increase of the fluid pressure the crack propagates along the direction of the maximum horizontal geostress with the oblate spheroid shape.

6.5. Three-dimensional simulation of three simultaneous horizontal wellbore

A three-dimensional simulation with three simultaneous perforations is now considered and the geometry is shown in Fig. 10(a) with the size of 8.3 m × 4.1 m × 4.1 m. Three perforation clusters with the distance of 2 m are applied at the front side representing the horizontal wellbore. A symmetric condition is prescribed at the side with perforation clusters and the other sides are all mechanically fixed. The material parameters and the geostress are considered to be the same. The distribution of the fluid pressure at two-time steps are shown in Fig. 10(b) and (c). It can be observed that no crack develops at the center perforation while two cracks form at the two outer perforations at the primary stage which is basically the same as the 2D case. It is worth noting that at the final stage the two outside cracks halt to

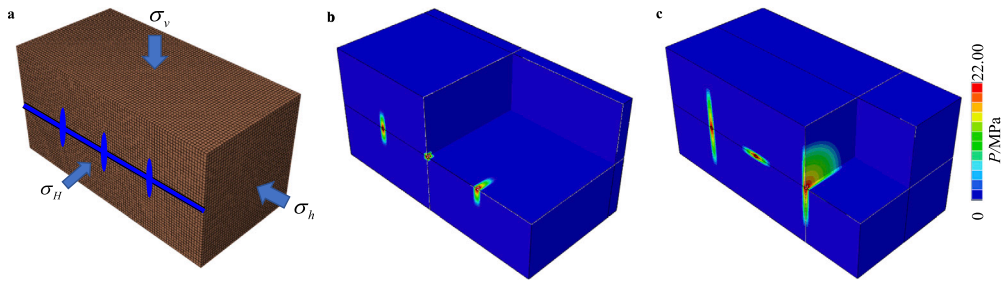

Fig. 10. Three-dimensional simulation of three simultaneous horizontal wellbore. (a) Geometry and in situ stress. Crack propagation and distribution of the fluid pressure at (b) primary stage. (c) final stage.

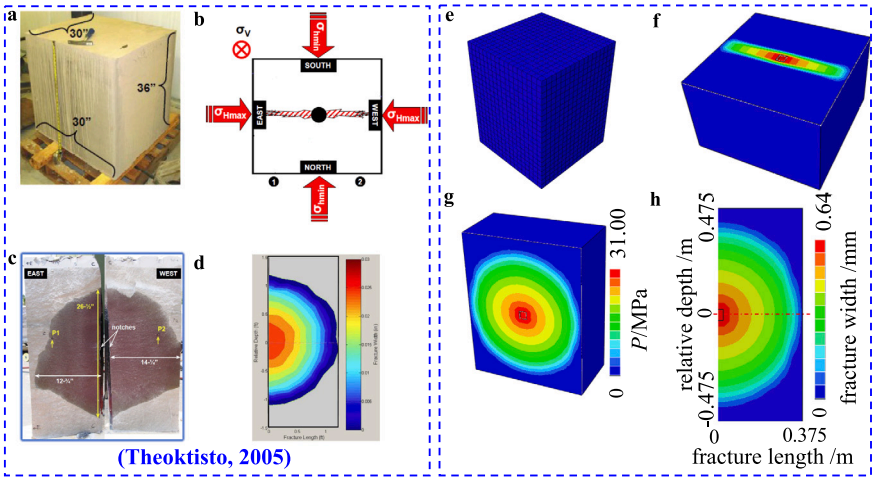

Fig. 11. Comparison with laboratory experiment of hydraulic fracturing. (a) Block of Colton sandstone. (b) Stress state. (c) Experimental results. (d) Simulation results of Casas Theoktisto (2005). (e) Numerical model. (f) Fracture shape on a horizontal section. (g) Fracture shape on a vertical section. (h) Profile of fracture length and width.

propagate but the perforation at the center region starts to develop horizontal crack. The reason of this phenomenon is that after the two outer cracks propagate the fluid pressure inside cracks starts to compress the region nearby the center perforation and the stress state is gradually changed. This finally leads to deflect the direction of the minimal principal stress of the center perforation and crack starts to propagate horizontally. This result is totally agreed with the one in the work of Olson (2008). It is therefore verified that the proposed method is capable of studying the interactions of 3D multiply hydraulic fracturing.

6.6. Comparison with laboratory tests

Knowing the restrictions of the former qualitative numerical examples, the numerical results of our proposed method is now briefly compared with a published laboratory hydraulic fracturing test and the detailed information is referred in the work of Casas Theoktisto (2005). The laboratory test was performed on a large block of Colton sandstone with a centralized hole with the stress state shown in Fig. 11(a) and (b). The experimental results in Fig. 11(c) clearly show two nearly symmetrical fracture wings on both sides of the wellbore and the fracture length and height are directly measured from the fracture profile. The numerical simulation in the work shows the modeled width profile of the fracture which matches well with the one from the test (see Fig. 11(d)).

In this paper it is modeled with the full block with the injection section located in the center and all the sides are mechanically fixed. The material parameters and the stress state take the same as the laboratory experiment. The numerical prediction of the proposed method is displayed in Fig. 11(e)(f)(g)(h) and note that the fluid pressure, the fracture shape, radius and width at the borehole are well reproduced. The fracture shape is visualized with a horizontal and a vertical cut and one can observe two symmetric fracture wings in the vertical cut. The fracture is transversely perpendicular to the direction of the minimum principal stress which is basically the same as the laboratory test. Fig. 11(h) shows the fracture shape with the measurement of the fracture length and width which matches equally well with the results of laboratory experiment. The numerical results also clearly show the breakdown pressure of the present method (31.09 MPa) is well agreed with the ones in the laboratory test (30.34 MPa). It also shows the modeled length and width profile of the fracture which also matches well with the one from the experiment test.

7. Conclusions

(1) This paper establishes an analogy between hydraulic fracturing and heat conduction for simulating the fully coupled hydro-mechanical behavior. Based on this analogy, a simple numerical tool is developed in the framework of a commercial finite element package ABAQUS with two user-defined subroutines to characterize the fully coupling system. The proposed method is firstly verified by using the classical 2D-plain-strain KGD analytical solutions.

(2) It is then applied to study several typical hydraulic fracturing problems and laboratory tests. In the case of multiple simultaneous hydraulic cracking, it is found that stress interaction indeed has a strong influence on the ability to initiate fractures for finite perforations, but stability is the main reason for infinite ones. It is also noteworthy that the induced initial length of the perforations strongly affects the effects of stress interaction and stability.

(3) Since the development of the present method is restricted on the material level, the introduction of the virtual crack method coupled with elastic–brittle damage constitutive law is only the preliminary case

and can be further extended to other constitutive models that featured with coupled hydro-mechanical behavior. This method is expected to be a useful numerical tool to study the hydraulic fracturing due to its simplicity.

(4) Due to the limited space, there are still many issues in need of improvement in the future work, such as large size of the domain, effects of the mesh size, heterogeneity, etc. In the future, further investigations should consider more complex hydraulic fracturing behaviors, for example, the interaction between hydraulic fractures and natural discontinuities, hydraulic fracture branching etc. It is worth mentioning that the stepwise crack propagation behavior (Milanese et al., 2016) can be captured by our model which will be discussed in details in our future work.

CRediT authorship contribution statement

Mingyao Li: Conceptualization, Methodology, Validation, Formal analysis, Investigation, Writing – original draft, Writing – review & editing. **Dong Zhou:** Conceptualization, Supervision, Writing – review & editing. **Yewang Su:** Conceptualization, Methodology, Supervision, Project administration, Writing – review & editing.

Declaration of competing interest

The authors declare that they have no known competing financial interests or personal relationships that could have appeared to influence the work reported in this paper.

Data availability

Data will be made available on request.

Acknowledgments

Y.S. gratefully acknowledges the support from the National Natural Science Foundation of China (No. 12172359), Beijing Municipal Science and Technology Commission, China (Z191100002019010), Beijing Municipal Natural Science Foundation, China (No. 2202066), Key Research Program of Frontier Sciences of the Chinese Academy of Sciences, China (ZDBS-LY-JSC014),CAS Interdisciplinary Innovation Team, China (JCTD-2020-03), Strategic Priority Research Program of the Chinese Academy of Sciences, China (No. XDB22040501), and the State Key Laboratory of Structural Analysis for Industrial Equipment, Dalian University of Technology, China (No. GZ19102).

M.L. gratefully acknowledges the support from the National Natural Science Foundation of China for young scientist (No.11802332), Joint Fund of State Key Laboratory of Coal Resources and Safe Mining-the Beijing Outstanding Young Scientist Program, China (No. BJJWZYJH01 201911413037 and SKLCRSM21LH02), the China Scholarship Council (202206435003).

Appendix A. Virtual crack model

As a continuum approach for fracture mechanics, the virtual crack in the element is imagined taking place in the normal direction of the maximum principal strain exceeding the critical value. As the crack occurs, the element is assumed to be fully fractured in that direction corresponding to the brittle failure state of the elastic–brittle constitutive model, and thus the components of material stiffness matrix related to that direction are modified to zero. Three orthogonal cracks may appear in one element at most and the crack system is fixed as normal to the maximum principal strain at the time the cracks start to form and remain constant afterwards. However, the crack is assumed to be able to close and reopen according to the stress state, and the closed crack is able to support compressive loading but no shear ones. The material stiffness matrix is changed correspondingly as the crack opens and closes. The virtual crack method for shale formation is then fully presented in the following in the framework of finite element analysis.

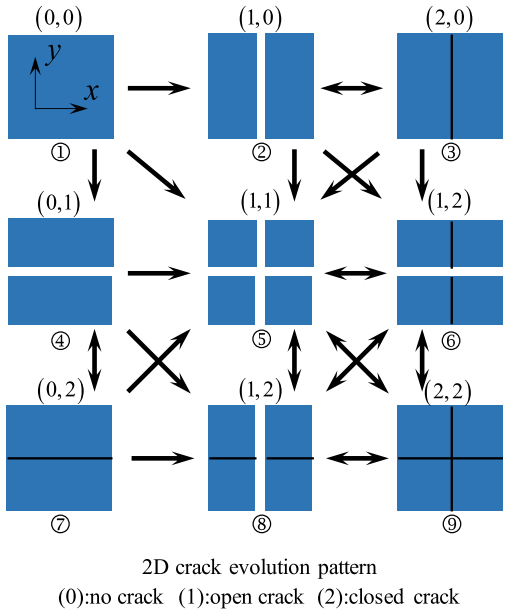

Fig. A.1. Illustration of the crack states and evolution pattern for a 2D orthogonal crack system.

Table A.1
State of 2D element and physical meaning with their opening and fracturing state.

State	Physical meaning	Opening state	Fracturing state
1	Intact	(0,0)	(0,0)
2	Cracked in 1st direction	(1,0)	(1,0)
3	Closed in 1st direction	(2,0)	(1,0)
4	Cracked in 2nd direction	(0,1)	(0,1)
5	Cracked in 1st and 2nd direction	(1,1)	(1,1)
6	Closed in 1st and cracked in 2nd direction	(2,1)	(1,1)
7	Closed in 2nd direction	(0,2)	(0,1)
8	Cracked in 1st and closed in 2nd direction	(1,2)	(1,1)
9	Closed in 1st and 2nd direction	(2,2)	(1,1)

A.1. State of element and its stiffness matrix

The two-dimensional case is firstly introduced with the assumption that all virtual cracks are parallel and normal to the coordinate axes. As shown in Fig. A.1, a 2D rectangular element has 9 definitive states with considering crack open and close. The state of each element is indicated by two opening state variables $(state1, state2)$, in which the state variables can be 0, 1 and 2 indicating intact, cracked and closed, correspondingly. At the same time, each element has two fracturing state variables (w_1, w_2), in which 0 denotes no crack and 1 opened or closed since the fluid is still allowed to flow within the closed crack. The state of 2D element and their physical meaning with their opening and fracturing state are summarized in the Table A.1.

As the state of element is defined, the stiffness matrix corresponding to certain state can be derived straightforward. Using the virtual crack conception, the crack starts to form in the direction normal to the principal strain exceeding the critical fracturing value. The stiffness matrix corresponding to that direction is then modified according to the element state. Thus, the stiffness matrix of the element is also definitive and relates uniquely to the state of that element. For instance, the element in state 1 is intact, so the corresponding stiffness matrix is completely same as the elastic stiffness matrix. The constitutive relation is $\sigma_i = D_{ij}^{[0,0]}\epsilon_j, i, j = 1, 2, \ldots, 6$, in which σ_i, ϵ_j are the stress and strain components and $D_{ij}^{[0,0]}$ is the stiffness matrix with the superscript $[0, 0]$ indicating the element on state 1. The stiffness matrix for the element

on state 1 is thus:

$$D^{[0,0]} = \begin{bmatrix} \lambda+2\mu & \lambda & \lambda & 0 & 0 & 0 \\ \lambda & \lambda+2\mu & \lambda & 0 & 0 & 0 \\ \lambda & \lambda & \lambda+2\mu & 0 & 0 & 0 \\ 0 & 0 & 0 & \mu & 0 & 0 \\ 0 & 0 & 0 & 0 & \mu & 0 \\ 0 & 0 & 0 & 0 & 0 & \mu \end{bmatrix} \tag{A.1}$$

As the critical fracturing strain has been reached, the state of element evolves with the stiffness matrix. For instance, as the strain in the 1st direction exceeds the critical fracturing value, the element on state 1 will evolve to state 2 which means the stress of the element in the 1st direction is zero as well as the shear stress relating to the 1st direction. Therefore, the constitutive relation becomes $\sigma_i = D_{ij}^{[1,0]}\varepsilon_j$ where $D_{ij}^{[1,0]}$ is the stiffness matrix relating to the element on state 2 with superscript indicator $[1,0]$, and takes the form:

$$D^{[0,0]} = \begin{bmatrix} \cancel{\lambda+2\mu} & \cancel{\lambda} & \cancel{\lambda} & 0 & 0 & 0 \\ \cancel{\lambda} & \lambda+2\mu & \lambda & 0 & 0 & 0 \\ \cancel{\lambda} & \lambda & \lambda+2\mu & 0 & 0 & 0 \\ 0 & 0 & 0 & \cancel{\mu} & 0 & 0 \\ 0 & 0 & 0 & 0 & \cancel{\mu} & 0 \\ 0 & 0 & 0 & 0 & 0 & \mu \end{bmatrix} \tag{A.2}$$

in which the cancel lines eliminate the normal and shear components corresponding to the fracturing direction. On the contrary, as the change of the stress condition the crack becomes closed, the state of the element will change from state 2 to state 3, which means that the normal direction of the closed crack recovers its ability for compression but not shear stress. Thus, the stiffness matrix of the element on state 3 becomes as follows:

$$D^{[0,0]} = \begin{bmatrix} \lambda+2\mu & \lambda & \lambda & 0 & 0 & 0 \\ \lambda & \lambda+2\mu & \lambda & 0 & 0 & 0 \\ \lambda & \lambda & \lambda+2\mu & 0 & 0 & 0 \\ 0 & 0 & 0 & \cancel{\mu} & 0 & 0 \\ 0 & 0 & 0 & 0 & \cancel{\mu} & 0 \\ 0 & 0 & 0 & 0 & 0 & \mu \end{bmatrix} \tag{A.3}$$

in which the blue one denotes the recovered components while the cancel lines eliminate the shear components. Following the same rules, the stiffness matrices for other states of elements are given in Appendix B.

A.2. Evolution rules

As shown in Fig. A.1 that the nine states of element can be evolved from one to another with the change of the stress state. However, it must be pointed out that the evolution of 2D element states must follow the rule (black arrow) shown in Fig. A.1. For example, the element can evolve from state 1 to state 2, 4 and 5, while from state 5 to 6, 8 and 9. It seems complicated, but there are certain rules to follow. The state of an element can only evolve from "intact" to "cracked" and then to "closed", and it can never change directly from "intact" to "closed". However, the "cracked" and "closed" can be interconverted but never back to "intact". The evolution rules can be clearly summarized in the Table A.2.

A.3. Criterion of evolution

As the evolution rules are set, the main challenge is to determine the criterion of evolution and determination of final state. As stated above, three states i.e. intact, cracked and closed, are possible, so the criterion of evolution is required to determine when the element will be cracked and closed. Using the virtual crack conception, the maximum principal strain criterion is adopted to determine whether the element should start to crack, while the criterion for distinguishing "cracked" or "closed" can be only decided by the stress condition. As long as the element is cracked in one direction, the normal stress relating to that direction is only possible to be less equal to zero. Thus, as the critical strain corresponding to zero normal stress is determined, the state of "cracked" or "closed" can be then confirmed.

Table A.2
Evolution rules of 2D element.

Initial state	Possible evolved state
1	2,4,5
2	3,5,6
3	2,5,6
4	5,7,8
5	6,8,9
6	5,8,9
7	4,5,8
8	5,6,9
9	5,6,8

For example, the initial state of an intact element at the current time is 1 which can be obtained from the opening state variables $(state1, state2) = (0,0)$, and the constitutive relations is $\sigma_{i(0)} = D_{ij}^{[0,0]}\varepsilon_{j(0)}$ (subscript 0 denotes the current time). In order to decide the state at subsequent time, the maximum principal strain criterion is firstly applied to the two directions by checking if the known strains $\varepsilon_{1(s)}, \varepsilon_{2(s)}$ (subscript s denotes subsequent time) at the subsequent time exceed the critical strain ε_c. The procedure can be detailed in the following:

(1) if $\varepsilon_{1(s)} \geq \varepsilon_c$ and $\varepsilon_{2(s)} < \varepsilon_c \Rightarrow$ state 2: $(state1, state2) = (1,0), (w_1, w_2) = (1,0)$
(2) if $\varepsilon_{2(s)} \geq \varepsilon_c$ and $\varepsilon_{1(s)} < \varepsilon_c \Rightarrow$ state 4: $(state1, state2) = (0,1), (w_1, w_2) = (0,1)$
(3) if $\varepsilon_{1(s)} \geq \varepsilon_c$ and $\varepsilon_{2(s)} \geq \varepsilon_c \Rightarrow$ state 5: $(state1, state2) = (1,1), (w_1, w_2) = (1,1)$
(4) other cases $\Rightarrow$ remain state1: $(state1, state2) = (0,0), (w_1, w_2) = (0,0)$

With such procedure the subsequent state of the element is well-determined, and the state is recorded by the state variables $(state1, state2)$ until the state is changed. At the same time, the subsequent constitutive relations are determined as $\boldsymbol{\sigma}_{(s)} = \boldsymbol{D}^{[state1,state2]}\boldsymbol{\varepsilon}_{(s)}$ where $\boldsymbol{D}^{[state1,state2]}$ is the new stiffness matrix corresponding to the new state of the element. It is worth noting that if the element is cracked the stress is zero while if it is closed the stress will not. Following the critical stress criterion, the state of element for either cracked or closed can be well-defined. For example, to decide whether the element on state 2 evolves to state 3, the stress in the 1st direction at the subsequent time is required to be checked. According to the constitutive relations at the subsequent time i.e. $\sigma_{1(s)} = (\lambda+2\mu)\varepsilon_{1(s)} + \lambda\varepsilon_{2(s)}$ ($\varepsilon_3 \equiv 0$ for plane strain problem), the critical strain can be derived according to zero stress criterion $\sigma_{1(s)} = 0$ as $\varepsilon'_{1(s)} = -[\lambda/(\lambda+2\mu)]\varepsilon_{2(s)}$. In other words, the element is closed only if $\varepsilon_{1(s)} \leq \varepsilon'_{1(s)}$, otherwise it remains open. Similarly, the critical strain for the 2nd direction is $\varepsilon'_{2(s)} = -[\lambda/(\lambda+2\mu)]\varepsilon_{1(s)}$.

The state of the element at the current time is firstly obtained from the current state variable and the state of the element at the subsequent time is then determined with fracturing criterion and critical strain criterion according to the above procedure. According to the stated criterion, as the initial state of the element is specific, the subsequent state can be definitively determined. The state variables and the stresses coupled with the variables of the solid problems can be then updated for solving the fluid–solid coupled problems.

A.4. Extension to 3D case

For a 3D element, there are 27 states with "intact", "cracked" and "closed" states in each dimension as can be seen from Fig. A.2. Similarly, the state of a 3D element can be indicated by three state variables denoting via $(state1, state2, state3)$, in which 0 indicates for

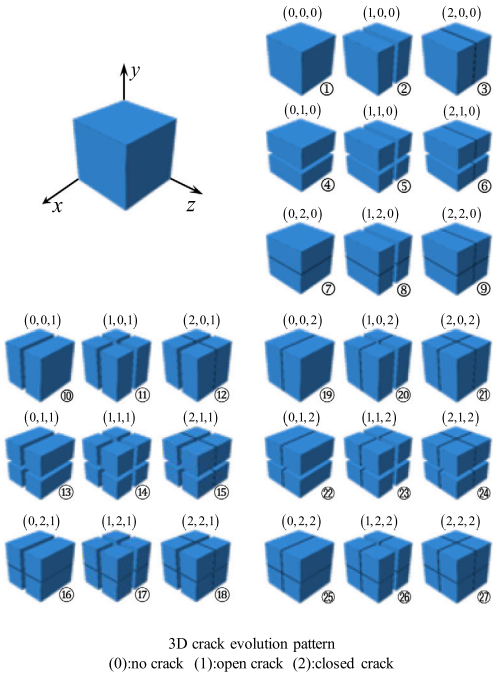

Fig. A.2. Illustration of the crack states and evolution pattern for 3D orthogonal crack system.

Table A.3
Evolution rules of 2D element.

Initial state	Possible evolved states
1	2,4,5,10,11,13,14
2	3,5,6,11,12,14,15
3	2,5,6,11,12,14,15
4	5,7,8,13,14,16,17
5	6,8,9,14,15,17,18
6	5,8,9,14,15,17,18
7	4,5,8,13,14,16,17
8	5,6,9,14,15,17,18
9	5,6,8,14,15,17,18
10	11,13,14,19,20,22,23
11	12,14,15,20,21,23,24
12	11,14,15,20,21,23,24
13	14,16,17,22,23,25,26
14	15,17,18,23,24,26,27
15	14,17,18,23,24,26,27
16	13,14,17,22,23,25,26
17	14,15,18,23,24,26,27
18	14,15,17,23,24,26,27
19	10,11,13,14,20,22,23
20	11,12,14,15,21,23,24
21	11,12,14,15,20,23,24
22	13,14,16,17,23,25,26
23	14,15,17,18,24,26,27
24	14,15,17,18,23,26,27
25	13,14,16,17,22,23,26
26	14,15,17,18,23,24,27
27	14,15,17,18,23,24,26

intact, 1 for cracked and 2 for closed. Correspondingly, the fracture state can be specifies using (w_1, w_2, w_3), in which 0 signifies intact and 1 for cracked/closed. The physical meaning of the state of element and fracture is exactly the same as the 2D case. It is noted that the evolution of the state of 3D element also follows the specific rules.

For example, the element is initially at state 1 (intact), the constitutive relation can be expressed as $\boldsymbol{\sigma} = \boldsymbol{D}^{[0,0,0]}\boldsymbol{\varepsilon}$, in which $\boldsymbol{D}^{[0,0,0]}$ is the stiffness matrix corresponding to state 1. Differently from 2D case, three state variables are required to indicate the state of 3D element. Similarly, the constitutive relation of a specific element is determined by changing the stiffness matrix according to the state of the element. For example, eliminate the normal and shear components corresponding to the cracked direction and recover the normal components relating to closed direction. The complete form of stiffness matrix corresponding to each state of element is detailed in Appendix B.

The evolution of 3D element is much more complicated comparing the 2D case. The element at state 1 has 7 possible states to evolve, i.e. 2, 4, 5, 10, 11, 13, 14. Similarly, the element at state 14 has 7 possible states as well, i.e. 15, 17, 18, 23, 24, 26, 27. However, the evolution is still systematic. The state of element in one direction can only evolve from "intact" to "cracked" and then to "closed". It is not possible from "intact" to "closed", but "cracked" and "closed" can be exchanged mutually. Meanwhile, as the element is cracked, it is not allowed "cracked" or "closed" back to "intact". Therefore, the evolution of 3D element can be systematized in Table A.3.

The criterion to determine whether the element is "intact", "cracked" or "closed" is based on the strain as same as the 2D cases. The maximum principal strain criterion can be used to check if the crack starts to form. In other words, it is used to distinguish the state of "intact" and "cracked". On the other hand, the state of "cracked" and "closed" can be only determined by the stress condition. Specifically, as the element has been cracked, the normal stress in the cracked direction can be only zero or negative which means only compressive and shear loads is allowed as the state of "cracked" changes to "closed". Therefore, the critical condition for stress equals to zero can be used to determine the critical state of "cracked" and "closed".

For example, the element at state 1 at the current time can be decided according to the current state variables $(0,0,0)$ denoting $(state1, state2, state3)$ with the current constitutive relation $\boldsymbol{\sigma}_{(0)} = \boldsymbol{D}^{[0,0,0]}\boldsymbol{\varepsilon}_{(0)}$ (subscript 0 signifying current time). In order to determine the state of the element at the subsequent time, it is required to check if crack occurs in any direction. For the case of cracks normal or along to the axes, it is necessary to check if the strain components $\varepsilon_{1(s)}, \varepsilon_{2(s)}, \varepsilon_{3(s)}$ (s represents the subsequent time) corresponding to the axes at the subsequent time exceeds the critical fracture strain ε_c to determine the state of the element at the subsequent time. For the element at state 1, the state at subsequent time can be determine as follows:

(1) $\varepsilon_{1(s)} \geq \varepsilon_c, \varepsilon_{2(s)} < \varepsilon_c, \varepsilon_{3(s)} < \varepsilon_c \Rightarrow$ state 2: $state = (1,0,0), w = (1,0,0)$
(2) $\varepsilon_{1(s)} < \varepsilon_c, \varepsilon_{2(s)} \geq \varepsilon_c, \varepsilon_{3(s)} < \varepsilon_c \Rightarrow$ state 4: $state = (0,1,0), w = (0,1,0)$
(3) $\varepsilon_{1(s)} \geq \varepsilon_c, \varepsilon_{2(s)} \geq \varepsilon_c, \varepsilon_{3(s)} < \varepsilon_c \Rightarrow$ state 5: $state = (1,1,0), w = (1,1,0)$
(4) $\varepsilon_{1(s)} < \varepsilon_c, \varepsilon_{2(s)} < \varepsilon_c, \varepsilon_{3(s)} \geq \varepsilon_c \Rightarrow$ state 10: $state = (0,0,1), w = (0,0,1)$
(5) $\varepsilon_{1(s)} \geq \varepsilon_c, \varepsilon_{2(s)} < \varepsilon_c, \varepsilon_{3(s)} \geq \varepsilon_c \Rightarrow$ state 11: $state = (1,0,1), w = (1,0,1)$
(6) $\varepsilon_{1(s)} < \varepsilon_c, \varepsilon_{2(s)} \geq \varepsilon_c, \varepsilon_{3(s)} \geq \varepsilon_c \Rightarrow$ state 13: $state = (0,1,1), w = (0,1,1)$
(7) $\varepsilon_{1(s)} \geq \varepsilon_c, \varepsilon_{2(s)} \geq \varepsilon_c, \varepsilon_{3(s)} \geq \varepsilon_c \Rightarrow$ state 14: $state = (1,1,1), w = (1,1,1)$
(8) otherwise$\Rightarrow$ remain state 1: $state = (0,0,0), w = (0,0,0)$

With such procedure, the state of the element at subsequent time can be definitively determined with the corresponding stiffness matrix simply obtaining from the state variables, and the constitutive relation is thus

$\boldsymbol{\sigma}_{(s)} = \boldsymbol{D}^{[state1, state2, state3]}\boldsymbol{\varepsilon}_{(s)}$.

It is noteworthy that whether the element is "cracked" or "closed" should be further investigated if the element has been cracked. For example, to determine whether the element at state 2 evolves to state 3 or not, it is required to utilize the critical stress condition to prejudge the state at subsequent time. From the critical stress condition, one has

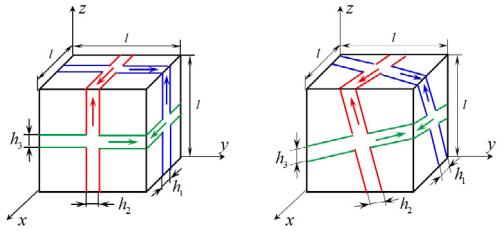

Fig. A.3. Illustration of arbitrary crack propagation path.

$\sigma_{1(s)} = 0$ in the 1st direction which can be expressed as the constitutive relation as $\sigma_{1(s)} = (\lambda + 2\mu)\varepsilon_{1(s)} + \lambda(\varepsilon_{2(s)} + \varepsilon_{3(s)})$ and the critical strain can be deduced as $\varepsilon'_{1(s)} = -[\lambda/(\lambda + 2\mu)](\varepsilon_{2(s)} + \varepsilon_{3(s)})$. In other words, in the case of no crack on the other two directions, the crack in the 1st direction is closed if $\varepsilon_{1(s)} \leq \varepsilon'_{1(s)}$, otherwise, it is open. It must be pointed out that the state of "open" or "closed" of an element in one direction depends on the state of the element on other two directions. For example, to determine whether the element on the state 2 evolves to state 5 or 6, one must find the critical strain on the condition that the element is cracked in the 2nd direction. Namely, the stress in the 2nd direction is zero, i.e. $\sigma_{2(s)} = (\lambda + 2\mu)\tilde{\varepsilon}_{2(s)} + \lambda(\varepsilon_{1(s)} + \varepsilon_{3(s)}) = 0$, in which $\tilde{\varepsilon}_{2(s)}$ is the trial strain which also determines the critical state in the 1st direction, i.e. $\sigma_{1(s)} = (\lambda+2\mu)\varepsilon_{1(s)}+\lambda(\tilde{\varepsilon}_{2(s)}+\varepsilon_{3(s)}) = 0$. In this case, the state of element in the 1st direction can be derived from these two critical conditions as $\varepsilon''_{1(s)} = -\nu\varepsilon_{3(s)}$ and then determine the subsequent state of the element at the state 2 initially. Specifically, it will evolve to state 5 if $\varepsilon_{1(s)} \geq \varepsilon''_{1(s)}$, and state 6 otherwise.

Similarly, the state of each element at the subsequent time can be definitively determined as well as the corresponding stiffness matrix with such procedure. With the definitive constitutive relation, the mechanical behaviors of the solid can be obtained and ready to be used in the coupling problems.

A.5. Arbitrary crack propagation path

For the sake of simplicity, the former criterion for both 2D and 3D is limited for the case that the crack propagates along/normal to the axes. However, it is easy to extend to the general case of arbitrary propagation path regardless the axes (Fig. A.3). For the general case, the crack forms normal to the maximum principal strain direction and the modified stiffness matrix is thus referring to the local coordinate axes corresponding to the principal strain direction. Therefore, the local stiffness matrix must be transformed to the global coordinates taking the form:

$$\boldsymbol{D}^G = \boldsymbol{T}\boldsymbol{D}^L\boldsymbol{T}^T \tag{A.4}$$

where $\boldsymbol{D}^G$ is the global stiffness matrix, $\boldsymbol{D}^L$ the local stiffness matrix and $\boldsymbol{T}$ the rotation matrix which is a function of principle direction. The explicit form of the rotation matrix can be found in Appendix C.

Appendix B. Stiffness matrix of cracked element

B.1. Stiffness matrices of 2D element

The stiffness matrices of 2D element are definitively defined according to the 9 states and each stiffness matrix matches one certain state of the element with the indicator of the superscript $[state1, state2]$. As longs as the state of the element is well-determined by the state variables, the stiffness matrix can be retrieved with the superscripts accordingly. The complete form of the stiffness matrices is listed as follows:

$$D^{[0,0]} = \begin{bmatrix} \lambda+2\mu & \lambda & \lambda & 0 & 0 & 0 \\ \lambda & \lambda+2\mu & \lambda & 0 & 0 & 0 \\ \lambda & \lambda & \lambda+2\mu & 0 & 0 & 0 \\ 0 & 0 & 0 & \mu & 0 & 0 \\ 0 & 0 & 0 & 0 & \mu & 0 \\ 0 & 0 & 0 & 0 & 0 & \mu \end{bmatrix} \tag{B.1}$$

$$D^{[1,0]} = \begin{bmatrix} 0 & 0 & 0 & 0 & 0 & 0 \\ 0 & \lambda+2\mu & \lambda & 0 & 0 & 0 \\ 0 & \lambda & \lambda+2\mu & 0 & 0 & 0 \\ 0 & 0 & 0 & 0 & 0 & 0 \\ 0 & 0 & 0 & 0 & 0 & 0 \\ 0 & 0 & 0 & 0 & 0 & \mu \end{bmatrix} \tag{B.2}$$

$$D^{[2,0]} = \begin{bmatrix} \lambda+2\mu & \lambda & \lambda & 0 & 0 & 0 \\ \lambda & \lambda+2\mu & \lambda & 0 & 0 & 0 \\ \lambda & \lambda & \lambda+2\mu & 0 & 0 & 0 \\ 0 & 0 & 0 & 0 & 0 & 0 \\ 0 & 0 & 0 & 0 & 0 & 0 \\ 0 & 0 & 0 & 0 & 0 & \mu \end{bmatrix} \tag{B.3}$$

$$D^{[0,1]} = \begin{bmatrix} \lambda+2\mu & 0 & 0 & 0 & 0 & 0 \\ 0 & 0 & 0 & 0 & 0 & 0 \\ \lambda & 0 & \lambda+2\mu & 0 & 0 & 0 \\ 0 & 0 & 0 & 0 & 0 & 0 \\ 0 & 0 & 0 & 0 & \mu & 0 \\ 0 & 0 & 0 & 0 & 0 & 0 \end{bmatrix} \tag{B.4}$$

$$D^{[1,1]} = \begin{bmatrix} 0 & 0 & 0 & 0 & 0 & 0 \\ 0 & 0 & 0 & 0 & 0 & 0 \\ 0 & 0 & \lambda+2\mu & 0 & 0 & 0 \\ 0 & 0 & 0 & 0 & 0 & 0 \\ 0 & 0 & 0 & 0 & 0 & 0 \\ 0 & 0 & 0 & 0 & 0 & 0 \end{bmatrix} \tag{B.5}$$

$$D^{[2,1]} = \begin{bmatrix} \lambda+2\mu & 0 & \lambda & 0 & 0 & 0 \\ 0 & 0 & 0 & 0 & 0 & 0 \\ \lambda & 0 & \lambda+2\mu & 0 & 0 & 0 \\ 0 & 0 & 0 & 0 & 0 & 0 \\ 0 & 0 & 0 & 0 & 0 & 0 \\ 0 & 0 & 0 & 0 & 0 & 0 \end{bmatrix} \tag{B.6}$$

$$D^{[0,2]} = \begin{bmatrix} \lambda+2\mu & \lambda & \lambda & 0 & 0 & 0 \\ \lambda & \lambda+2\mu & \lambda & 0 & 0 & 0 \\ \lambda & \lambda & \lambda+2\mu & 0 & 0 & 0 \\ 0 & 0 & 0 & 0 & 0 & 0 \\ 0 & 0 & 0 & 0 & \mu & 0 \\ 0 & 0 & 0 & 0 & 0 & 0 \end{bmatrix} \tag{B.7}$$

$$D^{[1,2]} = \begin{bmatrix} 0 & 0 & 0 & 0 & 0 & 0 \\ 0 & \lambda+2\mu & \lambda & 0 & 0 & 0 \\ 0 & \lambda & \lambda+2\mu & 0 & 0 & 0 \\ 0 & 0 & 0 & 0 & 0 & 0 \\ 0 & 0 & 0 & 0 & 0 & 0 \\ 0 & 0 & 0 & 0 & 0 & 0 \end{bmatrix} \tag{B.8}$$

$$D^{[2,2]} = \begin{bmatrix} \lambda+2\mu & \lambda & \lambda & 0 & 0 & 0 \\ \lambda & \lambda+2\mu & \lambda & 0 & 0 & 0 \\ \lambda & \lambda & \lambda+2\mu & 0 & 0 & 0 \\ 0 & 0 & 0 & 0 & 0 & 0 \\ 0 & 0 & 0 & 0 & 0 & 0 \\ 0 & 0 & 0 & 0 & 0 & 0 \end{bmatrix} \tag{B.9}$$

B.2. Stiffness matrices of 3D element

The stiffness matrices of 3D element are definitively defined according to the 27 states and each stiffness matrix matches one certain state of the element with the indicator of the superscript [$state1, state2, state3$]. Some of the matrices corresponding to different state of element take the same form due to the analogy of the crack system, and the stiffness matrices are listed in the same equation for the sake of concision but with different indicators. As longs as the state of the element is well-determined by the state variables, the stiffness matrix can be retrieved with the superscripts accordingly. The complete form of the stiffness matrices is listed as follows:

$$D^{[0,0,0]} = \begin{bmatrix} \lambda+2\mu & \lambda & \lambda & 0 & 0 & 0 \\ \lambda & \lambda+2\mu & \lambda & 0 & 0 & 0 \\ \lambda & \lambda & \lambda+2\mu & 0 & 0 & 0 \\ 0 & 0 & 0 & \mu & 0 & 0 \\ 0 & 0 & 0 & 0 & \mu & 0 \\ 0 & 0 & 0 & 0 & 0 & \mu \end{bmatrix} \tag{B.10}$$

$$D^{[1,0,0]} = \begin{bmatrix} 0 & 0 & 0 & 0 & 0 & 0 \\ 0 & \lambda+2\mu & \lambda & 0 & 0 & 0 \\ 0 & \lambda & \lambda+2\mu & 0 & 0 & 0 \\ 0 & 0 & 0 & 0 & 0 & 0 \\ 0 & 0 & 0 & 0 & 0 & 0 \\ 0 & 0 & 0 & 0 & 0 & \mu \end{bmatrix} \tag{B.11}$$

$$D^{[0,1,0]} = \begin{bmatrix} \lambda+2\mu & 0 & 0 & 0 & 0 & 0 \\ 0 & 0 & 0 & 0 & 0 & 0 \\ \lambda & 0 & \lambda+2\mu & 0 & 0 & 0 \\ 0 & 0 & 0 & 0 & 0 & 0 \\ 0 & 0 & 0 & 0 & \mu & 0 \\ 0 & 0 & 0 & 0 & 0 & 0 \end{bmatrix} \tag{B.12}$$

$$D^{[1,1,0]} = D^{[1,1,2]} = \begin{bmatrix} 0 & 0 & 0 & 0 & 0 & 0 \\ 0 & 0 & 0 & 0 & 0 & 0 \\ 0 & 0 & \lambda+2\mu & 0 & 0 & 0 \\ 0 & 0 & 0 & 0 & 0 & 0 \\ 0 & 0 & 0 & 0 & 0 & 0 \\ 0 & 0 & 0 & 0 & 0 & 0 \end{bmatrix} \tag{B.13}$$

$$D^{[2,1,0]} = D^{[2,1,2]} = D^{[0,1,2]} = \begin{bmatrix} \lambda+2\mu & 0 & \lambda & 0 & 0 & 0 \\ 0 & 0 & 0 & 0 & 0 & 0 \\ \lambda & 0 & \lambda+2\mu & 0 & 0 & 0 \\ 0 & 0 & 0 & 0 & 0 & 0 \\ 0 & 0 & 0 & 0 & 0 & 0 \\ 0 & 0 & 0 & 0 & 0 & 0 \end{bmatrix} \tag{B.14}$$

$$D^{[0,2,0]} = \begin{bmatrix} \lambda+2\mu & \lambda & \lambda & 0 & 0 & 0 \\ \lambda & \lambda+2\mu & \lambda & 0 & 0 & 0 \\ \lambda & \lambda & \lambda+2\mu & 0 & 0 & 0 \\ 0 & 0 & 0 & 0 & 0 & 0 \\ 0 & 0 & 0 & 0 & \mu & 0 \\ 0 & 0 & 0 & 0 & 0 & 0 \end{bmatrix} \tag{B.15}$$

$$D^{[1,2,0]} = D^{[1,0,2]} = D^{[1,2,2]} = \begin{bmatrix} 0 & 0 & 0 & 0 & 0 & 0 \\ 0 & \lambda+2\mu & \lambda & 0 & 0 & 0 \\ 0 & \lambda & \lambda+2\mu & 0 & 0 & 0 \\ 0 & 0 & 0 & 0 & 0 & 0 \\ 0 & 0 & 0 & 0 & 0 & 0 \\ 0 & 0 & 0 & 0 & 0 & 0 \end{bmatrix} \tag{B.16}$$

$$D^{[2,2,0]} = D^{[2,0,2]} = D^{[0,2,2]} = D^{[2,2,2]} = \begin{bmatrix} \lambda+2\mu & \lambda & \lambda & 0 & 0 & 0 \\ \lambda & \lambda+2\mu & \lambda & 0 & 0 & 0 \\ \lambda & \lambda & \lambda+2\mu & 0 & 0 & 0 \\ 0 & 0 & 0 & 0 & 0 & 0 \\ 0 & 0 & 0 & 0 & 0 & 0 \\ 0 & 0 & 0 & 0 & 0 & 0 \end{bmatrix} \tag{B.17}$$

$$D^{[0,0,1]} = \begin{bmatrix} \lambda+2\mu & \lambda & 0 & 0 & 0 & 0 \\ \lambda & \lambda+2\mu & 0 & 0 & 0 & 0 \\ 0 & 0 & 0 & 0 & 0 & 0 \\ 0 & 0 & 0 & \mu & 0 & 0 \\ 0 & 0 & 0 & 0 & 0 & 0 \\ 0 & 0 & 0 & 0 & 0 & 0 \end{bmatrix} \tag{B.18}$$

$$D^{[1,0,1]} = D^{[1,2,1]} = \begin{bmatrix} 0 & 0 & 0 & 0 & 0 & 0 \\ 0 & \lambda+2\mu & 0 & 0 & 0 & 0 \\ 0 & 0 & 0 & 0 & 0 & 0 \\ 0 & 0 & 0 & 0 & 0 & 0 \\ 0 & 0 & 0 & 0 & 0 & 0 \\ 0 & 0 & 0 & 0 & 0 & 0 \end{bmatrix} \tag{B.19}$$

$$D^{[2,0,1]} = D^{[0,2,1]} = D^{[2,2,1]} = \begin{bmatrix} \lambda+2\mu & \lambda & 0 & 0 & 0 & 0 \\ \lambda & \lambda+2\mu & 0 & 0 & 0 & 0 \\ 0 & 0 & 0 & 0 & 0 & 0 \\ 0 & 0 & 0 & 0 & 0 & 0 \\ 0 & 0 & 0 & 0 & 0 & 0 \\ 0 & 0 & 0 & 0 & 0 & 0 \end{bmatrix} \tag{B.20}$$

$$D^{[0,1,1]} = D^{[2,1,1]} = \begin{bmatrix} \lambda+2\mu & 0 & 0 & 0 & 0 & 0 \\ 0 & 0 & 0 & 0 & 0 & 0 \\ 0 & 0 & 0 & 0 & 0 & 0 \\ 0 & 0 & 0 & 0 & 0 & 0 \\ 0 & 0 & 0 & 0 & 0 & 0 \\ 0 & 0 & 0 & 0 & 0 & 0 \end{bmatrix} \tag{B.21}$$

$$D^{[1,1,1]} = \begin{bmatrix} 0 & 0 & 0 & 0 & 0 & 0 \\ 0 & 0 & 0 & 0 & 0 & 0 \\ 0 & 0 & 0 & 0 & 0 & 0 \\ 0 & 0 & 0 & 0 & 0 & 0 \\ 0 & 0 & 0 & 0 & 0 & 0 \\ 0 & 0 & 0 & 0 & 0 & 0 \end{bmatrix} \tag{B.22}$$

$$D^{[0,0,2]} = \begin{bmatrix} \lambda+2\mu & \lambda & \lambda & 0 & 0 & 0 \\ \lambda & \lambda+2\mu & \lambda & 0 & 0 & 0 \\ \lambda & \lambda & \lambda+2\mu & 0 & 0 & 0 \\ 0 & 0 & 0 & \mu & 0 & 0 \\ 0 & 0 & 0 & 0 & 0 & 0 \\ 0 & 0 & 0 & 0 & 0 & 0 \end{bmatrix} \tag{B.23}$$

$$D^{[2,0,0]} = \begin{bmatrix} \lambda+2\mu & \lambda & \lambda & 0 & 0 & 0 \\ \lambda & \lambda+2\mu & \lambda & 0 & 0 & 0 \\ \lambda & \lambda & \lambda+2\mu & 0 & 0 & 0 \\ 0 & 0 & 0 & 0 & 0 & 0 \\ 0 & 0 & 0 & 0 & 0 & 0 \\ 0 & 0 & 0 & 0 & 0 & \mu \end{bmatrix} \tag{B.24}$$

Appendix C. Rotation matrix of crack system

As long as the maximum principal strain is found and the first crack forms, the crack system is fixed to be three mutually orthogonal directions even though the other two cracks does not exist. In other words, the other two cracks are only possible to form in the directions orthogonal to the first one and mutually orthogonal to each other. The directions of the crack system are the direction of the principle

strain when the first crack occurs, and the direction $\boldsymbol{n}_k = n_{ki}\boldsymbol{e}_i$ can be expressed as:

$$n_{ki} = \begin{bmatrix} n_{11} & n_{12} & n_{13} \\ n_{21} & n_{22} & n_{23} \\ n_{31} & n_{32} & n_{33} \end{bmatrix} \tag{C.1}$$

which determines the local coordinate axes corresponding to the crack system. The stiffness matrices listed previously are naturally according to the local coordinate axes. Thus, for the constitutive relations in the arbitrary cases, the local stiffness matrices must of course be transformed to the global coordinates, taking the form $\boldsymbol{\sigma} = \boldsymbol{D}^G\boldsymbol{\varepsilon}$, in which $\boldsymbol{D}^G = \boldsymbol{T}\boldsymbol{D}^L\boldsymbol{T}^T$ and $\boldsymbol{D}^G$ is the global stiffness matrix and $\boldsymbol{D}^L$ is the local one. The rotation matrix $\boldsymbol{T}$ is the function of the crack system directions and the general form can be expressed as:

$$\boldsymbol{T} = \begin{bmatrix} n_{11}^2 & n_{12}^2 & n_{13}^2 & n_{11}n_{12} & n_{11}n_{12} & n_{12}n_{13} \\ n_{21}^2 & n_{22}^2 & n_{23}^2 & n_{21}n_{22} & n_{21}n_{23} & n_{22}n_{23} \\ n_{31}^2 & n_{32}^2 & n_{33}^2 & n_{31}n_{32} & n_{31}n_{33} & n_{32}n_{33} \\ 2n_{11}n_{21} & 2n_{12}n_{22} & 2n_{13}n_{23} & n_{12}n_{21}+n_{11}n_{22} & n_{13}n_{21}+n_{11}n_{23} & n_{13}n_{22}+n_{12}n_{23} \\ 2n_{11}n_{31} & 2n_{12}n_{32} & 2n_{13}n_{33} & n_{12}n_{31}+n_{11}n_{32} & n_{13}n_{31}+n_{11}n_{33} & n_{13}n_{32}+n_{12}n_{33} \\ 2n_{21}n_{31} & 2n_{22}n_{32} & 2n_{23}n_{33} & n_{22}n_{31}+n_{21}n_{32} & n_{21}n_{33}+n_{23}n_{31} & n_{22}n_{33}+n_{23}n_{32} \end{bmatrix} \tag{C.2}$$

References

Adachi, J., Siebrits, E., Peirce, A., Desroches, J., 2007. Computer simulation of hydraulic fractures. Int. J. Rock Mech. Min. Sci. 44 (5), 739–757. http://dx.doi.org/10.1016/j.ijrmms.2006.11.006, URL: https://www.sciencedirect.com/science/article/pii/S1365160906001870.

Al-Busaidi, A., 2005. Distinct element modeling of hydraulically fractured Lac du Bonnet granite. J. Geophys. Res. Solid Earth 110 (B6302), 1–14. http://dx.doi.org/10.1029/2004JB003297.

Barboza, B.R., Chen, B., Li, C., 2021. A review on proppant transport modelling. J. Pet. Sci. Eng. 204, 108753. http://dx.doi.org/10.1016/j.petrol.2021.108753, URL: https://www.sciencedirect.com/science/article/pii/S0920410521004137.

Bažant, Z.P., Ohtsubo, H., 1977. Stability conditions for propagation of a system of cracks in a brittle solid. Mech. Res. Commun. 4 (5), 353–366. http://dx.doi.org/10.1016/0093-6413(77)90015-5, URL: https://www.sciencedirect.com/science/article/pii/0093641377900155.

Bažant, Z.P., Ohtsubo, H., Aoh, K., 1979. Stability and post-critical growth of a system of cooling or shrinkage cracks. Int. J. Fract. 15 (5), 443–456.

Bažant, Z.P., Salviato, M., Chau, V.T., Viswanathan, H., Zubelewicz, A., 2014. Why fracking works. J. Appl. Mech. 81 (10), http://dx.doi.org/10.1115/1.4028192, 101010. arXiv:https://asmedigitalcollection.asme.org/appliedmechanics/article-pdf/81/10/101010/6080048/jam_081_10_101010.pdf.

Carrier, B., Granet, S., 2012. Numerical modeling of hydraulic fracture problem in permeable medium using cohesive zone model. Eng. Fract. Mech. 79, 312–328. http://dx.doi.org/10.1016/j.engfracmech.2011.11.012, URL: https://www.sciencedirect.com/science/article/pii/S0013794411004206.

Casas Theoktisto, L.A., 2005. Large scale hydraulic fracturing test on a rock with artificial discontinuities. URL: http://hdl.handle.net/11124/79074.

Chau, V.T., Bažant, Z.P., Su, Y., 2016. Growth model for large branched three-dimensional hydraulic crack system in gas or oil shale. Phil. Trans. R. Soc. A 374 (2078), 20150418. http://dx.doi.org/10.1098/rsta.2015.0418, arXiv:https://royalsocietypublishing.org/doi/pdf/10.1098/rsta.2015.0418.

Chen, B., Sun, Y., Bai, J., Thomas, H.R., Dutko, M., Cottrell, M., Li, C., 2022. A review of hydraulic fracturing simulation. Arch. Comput. Methods Eng. 29, 1–58. http://dx.doi.org/10.1007/s11831-021-09653-z.

Chen, B., Sun, Y., Barboza, B.R., Barron, A.R., Li, C., 2020. Phase-field simulation of hydraulic fracturing with a revised fluid model and hybrid solver. Eng. Fract. Mech. 229, 106928. http://dx.doi.org/10.1016/j.engfracmech.2020.106928, URL: https://www.sciencedirect.com/science/article/pii/S0013794419310094.

Chung, B.-J., Chae, M.-S., Moon, J.-Y., Park, H.-K., 2021. Review of research using analogy concept for thermal hydraulic and severe accident experiments. Nucl. Eng. Des. 379, 111257. http://dx.doi.org/10.1016/j.nucengdes.2021.111257, URL: https://www.sciencedirect.com/science/article/pii/S0029549321002090.

Dershowitz, W., Cottrell, M., Lim, D., Doe, T., 2010. A Discrete Fracture Network Approach For Evaluation of Hydraulic Fracture Stimulation of Naturally Fractured Reservoirs. ARMA-10-475.

Detournay, E., 2004. Propagation regimes of fluid-driven fractures in impermeable rocks. Int. J. Geomech. 4 (1), 35–45. http://dx.doi.org/10.1061/(ASCE)1532-3641(2004)4:1(35).

Devloo, P.R., Fernandes, P.D., Gomes, S.M., Bravo, C.M.A.A., Damas, R.G., 2006. A finite element model for three dimensional hydraulic fracturing. Math. Comput. Simulation 73 (1), 142–155. http://dx.doi.org/10.1016/j.matcom.2006.06.020, URL: https://www.sciencedirect.com/science/article/pii/S0378475406001790. Applied and Computational Mathematics - Selected Papers of the Fifth PanAmerican Workshop - June 21-25, 2004, Tegucigalpa, Honduras.

Dong, C., de Pater, C., 2001. Numerical implementation of displacement discontinuity method and its application in hydraulic fracturing. Comput. Methods Appl. Mech. Engrg. 191 (8), 745–760. http://dx.doi.org/10.1016/S0045-7825(01)00273-0, URL: https://www.sciencedirect.com/science/article/pii/S0045782501002730.

Duan, Z., Zhang, J., An, Y., Jiang, H., 2013. Simulation of the transient behavior of gels based on an analogy between diffusion and heat transfer. J. Appl. Mech. 80 (4), http://dx.doi.org/10.1115/1.4007789, 041017. arXiv:https://asmedigitalcollection.asme.org/appliedmechanics/article-pdf/80/4/041017/6077334/jam_80_4_041017.pdf.

Fu, P., Johnson, S.M., Carrigan, C.R., 2013. An explicitly coupled hydro-geomechanical model for simulating hydraulic fracturing in arbitrary discrete fracture networks. Int. J. Numer. Anal. Methods Geomech. 37 (14).

Geertsma, J., de Klerk, F., 1969. Rapid method of predicting width and extent of hydraulically induced fractures. J. Pet. Technol. 21, http://dx.doi.org/10.2118/2458-PA, URL: https://www.osti.gov/biblio/5540178.

Gordeliy, E., Peirce, A., 2013. Implicit level set schemes for modeling hydraulic fractures using the XFEM. Comput. Methods Appl. Mech. Engrg. 266, 125–143. http://dx.doi.org/10.1016/j.cma.2013.07.016, URL: https://www.sciencedirect.com/science/article/pii/S0045782513001928.

Hao, L., Xu, F., Chen, Q., Wei, M., Chen, L., Min, Y., 2018. A thermal-electrical analogy transient model of district heating pipelines for integrated analysis of thermal and power systems. Appl. Therm. Eng. 139, 213–221. http://dx.doi.org/10.1016/j.applthermaleng.2018.04.124, URL: https://www.sciencedirect.com/science/article/pii/S1359431117374185.

Hu, Y., Chen, G., Cheng, W., Yang, Z., 2014. Simulation of hydraulic fracturing in rock mass using a smeared crack model. Comput. Struct. 137, 72–77. http://dx.doi.org/10.1016/j.compstruc.2013.04.011, URL: https://www.sciencedirect.com/science/article/pii/S0045794913001132. Special Issue Title: UK Association for Computational Mechanics in Engineering.

Hunsweck, M.J., Shen, Y., Lew, A.J., 2013. A finite element approach to the simulation of hydraulic fractures with lag. Int. J. Numer. Anal. Methods Geomech..

Josh, M., Esteban, L., Delle Piane, C., Sarout, J., Dewhurst, D., Clennell, M., 2012. Laboratory characterisation of shale properties. J. Pet. Sci. Eng. 88–89, 107–124. http://dx.doi.org/10.1016/j.petrol.2012.01.023, URL: https://www.sciencedirect.com/science/article/pii/S0920410512000411. Unconventional hydrocarbons exploration and production Challenges.

Kresse, O., Weng, X., Gu, H., Wu, R., 2013. Numerical modeling of hydraulic fractures interaction in complex naturally fractured formations. Rock Mech. Rock Eng. 46 (3), 555–568. http://dx.doi.org/10.1007/s00603-012-0359-2.

Lecampion, B., 2009. An extended finite element method for hydraulic fracture problems. Commun. Numer. Methods. Eng. 25 (2), 121–133.

Li, M., Chen, X., Zhou, D., Su, Y., 2020. A spectral microplane model for the anisotropic damage behavior of shales. J. Appl. Mech. 87 (8), http://dx.doi.org/10.1115/1.4047005, 081001. arXiv:https://asmedigitalcollection.asme.org/appliedmechanics/article-pdf/87/8/081001/6534947/jam_87_8_081001.pdf.

Li, M., Guo, P., Stolle, D., Liang, L., 2016. Development of hydraulic fracture zone in heterogeneous material based on smeared crack method. J. Natural Gas Sci. Eng. 35, 761–774. http://dx.doi.org/10.1016/j.jngse.2016.09.018, URL: https://www.sciencedirect.com/science/article/pii/S1875510016306588.

Miehe, C., Schänzel, L.-M., Ulmer, H., 2015. Phase field modeling of fracture in multi-physics problems. Part I. Balance of crack surface and failure criteria for brittle crack propagation in thermo-elastic solids. Comput. Methods Appl. Mech. Engrg. 294, 449–485. http://dx.doi.org/10.1016/j.cma.2014.11.016, URL: https://www.sciencedirect.com/science/article/pii/S0045782514004423.

Mikelic, A., Wheeler, M.F., Wick, T., 2015. Phase-field modeling of a fluid-driven fracture in a poroelastic medium. Comput. Geosci. 19 (6), 1171–1195.

Milanese, E., Rizzato, P., Pesavento, F., Secchi, S., Schrefler, B., 2016. An explanation for the intermittent crack tip advancement and pressure fluctuations in hydraulic fracturing. Hydraul. Fract. J. 3, 30–43.

Mitchell, S.L., Kuske, R., Peirce, A.P., 2006. An asymptotic framework for the analysis of hydraulic fractures: The impermeable case. J. Appl. Mech. 74 (2), 365–372. http://dx.doi.org/10.1115/1.2200653, arXiv:https://asmedigitalcollection.asme.org/appliedmechanics/article-pdf/74/2/365/5476587/365_1.pdf.

Mohammadnejad, T., Khoei, A., 2013. An extended finite element method for hydraulic fracture propagation in deformable porous media with the cohesive crack model. Finite Elem. Anal. Des. 73, 77–95. http://dx.doi.org/10.1016/j.finel.2013.05.005, URL: https://www.sciencedirect.com/science/article/pii/S0168874X13000772.

Montgomery, C.T., Smith, M.B., 2010. Hydraulic fracturing: History of an enduring technology. J. Pet. Technol. 62 (12), 26–40. http://dx.doi.org/10.2118/1210-0026-JPT, arXiv:https://onepetro.org/JPT/article-pdf/62/12/26/2207932/spe-1210-0026-jpt.pdf.

Olson, J., 2008. Multi-Fracture Propagation Modeling: applications to Hydraulic Fracturing in Shales and Tight Gas Sands. ARMA-08-327, arXiv:https://onepetro.org/ARMAUSRMS/proceedings-pdf/ARMA08/All-ARMA08/ARMA-08-327/1809290/arma-08-327.pdf.

Olson, J.E., Dahi-Taleghani, A., 2009. Modeling Simultaneous Growth of Multiple Hydraulic Fractures and Their Interaction With Natural Fractures. SPE-119739-MS, http://dx.doi.org/10.2118/119739-MS, arXiv:https://onepetro.org/SPEHFTC/proceedings-pdf/09HFTC/All-09HFTC/SPE-119739-MS/2706718/spe-119739-ms.pdf.

Osiptsov, A.A., 2017. Fluid mechanics of hydraulic fracturing: a review. J. Pet. Sci. Eng. 156, 513–535. http://dx.doi.org/10.1016/j.petrol.2017.05.019, URL: https://www.sciencedirect.com/science/article/pii/S0920410517304928.

Rahimi-Aghdam, S., Chau, V.-T., Lee, H., Nguyen, H., Li, W., Karra, S., Rougier, E., Viswanathan, H., Srinivasan, G., Bažant, Z.P., 2019. Branching of hydraulic cracks enabling permeability of gas or oil shale with closed natural fractures. Proc. Natl. Acad. Sci. 116 (5), 1532–1537. http://dx.doi.org/10.1073/pnas.1818529116, arXiv:https://www.pnas.org/doi/pdf/10.1073/pnas.1818529116.

Shimizu, H., Murata, S., Ishida, T., 2011. The distinct element analysis for hydraulic fracturing in hard rock considering fluid viscosity and particle size distribution. Int. J. Rock Mech. Min. Sci. 48 (5), 712–727. http://dx.doi.org/10.1016/j.ijrmms.2011.04.013, URL: https://www.sciencedirect.com/science/article/pii/S1365160911000669.

Sun, Y., Edwards, M.G., Chen, B., Li, C., 2021. A state-of-the-art review of crack branching. Eng. Fract. Mech. 257, 108036. http://dx.doi.org/10.1016/j.engfracmech.2021.108036, URL: https://www.sciencedirect.com/science/article/pii/S0013794421004550.

Wilson, Z.A., Landis, C.M., 2016. Phase-field modeling of hydraulic fracture. J. Mech. Phys. Solids 96, 264–290. http://dx.doi.org/10.1016/j.jmps.2016.07.019, URL: https://www.sciencedirect.com/science/article/pii/S002250961630285X.

Xie, L., Min, K.-B., Shen, B., 2016. Simulation of hydraulic fracturing and its interactions with a pre-existing fracture using displacement discontinuity method. J. Natural Gas Sci. Eng. 36, 1284–1294. http://dx.doi.org/10.1016/j.jngse.2016.03.050, URL: https://www.sciencedirect.com/science/article/pii/S1875510016301573. CSG2015 International Conference: China Shale and Coal Gases 2015.

Yao, Y., Liu, L., Keer, L.M., 2015. Pore pressure cohesive zone modeling of hydraulic fracture in quasi-brittle rocks. Mech. Mater. 83, 17–29. http://dx.doi.org/10.1016/j.mechmat.2014.12.010, URL: https://www.sciencedirect.com/science/article/pii/S0167663614002233.

Zeng, Q., Liu, Z., Wang, T., Gao, Y., Zhuang, Z., 2017. Fully coupled simulation of multiple hydraulic fractures to propagate simultaneously from a perforated horizontal wellbore. Comput. Mech..